



Prediction of surface urban heat island based on predicted consequences of urban sprawl using deep learning: A way forward for a sustainable environment

Shun Fu ^a, Lufeng Wang ^a, Umer Khalil ^b, Ali Hassan Cheema ^c, Israr Ullah ^d, Bilal Aslam ^e, Aqil Tariq ^{f,*}, Muhammad Aslam ^g, Saad S. Alarifi ^h

^a Chongqing Industry Polytechnic College, Chongqing, 1000 Taoyuan Avenue, Yu Bei District, Chongqing, 401120, China

^b ITC Faculty of Geo-Information Science and Earth Observation, University of Twente, 7522 NB, Enschede, the Netherlands

^c Department of Civil Engineering, COMSATS University Islamabad, Wah Campus, Islamabad, Pakistan

^d Neotectonics and Natural Hazards, RWTH Aachen University, Locknerstr, 4-20, 52056, Aachen, Germany

^e School of Informatics, Computing, and Cyber Systems, Northern Arizona University, Flagstaff, AZ, 86011, USA

^f Department of Wildlife, Fisheries and Aquaculture, College of Forest Resources, Mississippi State University, MS, 39762-9690, USA

^g Department of Computer Science Aberystwyth University, Penglais, Aberystwyth SY23 3DB, UK

^h Department of Geology and Geophysics, College of Science, King Saud University, P.O. Box 2455, Riyadh, 11451, Saudi Arabia

ARTICLE INFO

Keywords:

Convolutional neural network
Deep learning
Land surface temperature
Surface urban heat island

ABSTRACT

The present work aimed at the spatiotemporal analysis of Land Surface Temperature (LST) and several land-use land-cover spectral indices, namely Normalized Difference Vegetation Index (NDVI), Normalized Difference Built-up Index (NDBI), Soil Adjusted Vegetation Index (SAVI), and Modified Normalized Difference Water Index (MNDWI) and to develop a Convolutional Neural Network (CNN) model to predict the LST and the indices for Surface Urban Heat Island (SUHI) evaluation based on the impervious surface area. The predictions were made only for LST and two indices (NDVI and NDBI) because of their strong correlation with LST. Landsat-8 satellite imageries acquired for 2013, 2015, 2017, 2019, and 2021 were utilized, and the Sialkot district, a swiftly urbanizing and advancing industrial city, was selected as a case study area. In the study, first, the indices (NDVI and NDBI) were predicted for 2019, 2021, and 2023 following a sequential procedure, and then based on the predicted indices, the LST for the mentioned years was predicted. Ultimately, to analyze the impact of impervious area on SUHI, impervious and SUHI were extracted for 2019, 2021, and 2023 using the predicted NDBI and LST, respectively, by employing Otsu's Thresholding technique. The predicted LST and indices for 2019 and 2021 were compared with the obtained 2019 and 2021 LST and indices through several statistical measures, such as the kappa index, to evaluate the performance of the CNN model. The kappa index of different kappa statistics for 2019 and 2021 varied between 0.81 and 0.96, which resembles several previous studies, thus indicating sufficient future predictions. SUHI evaluation was conducted based on the observed (2016) and simulated (2021) impervious area and normalized LST images. The results showed that the distribution of the SUHI was highly related to the impervious area. Suppose the urbanization rate in the study area continues at its current pace. In that case, this expansion will cause a dramatic increase in SUHI distribution unless decision-makers consider any proper urban planning model for the study area.

•List of nomenclature

NDVI	Normalized Difference Vegetation Index	LST	Land Surface Temperature
------	--	-----	--------------------------

(continued on next column)

(continued)

NDBI	Normalized Difference Built-up Index	UHI	Urban Heat Island
------	--------------------------------------	-----	-------------------

(continued on next page)

* Corresponding author. Department of Wildlife, Fisheries and Aquaculture, College of Forest Resources, Mississippi State University, Mississippi State, MS, 39762-9690, USA.

E-mail address: at2139@msstate.edu (A. Tariq).

(continued)

SAVI	Soil Adjusted Vegetation Index	ISA	impervious surface area
MNDWI	Modified Normalized Difference Water Index	MODIS	Moderate Resolution Imaging Spectroradiometer
CNN	Convolutional Neural Network	ML	Machine Learning
SUHI	Surface Urban Heat Island	DL	Deep Learning
SVR	Support Vector Regression	ASTER	Advanced Spaceborne Thermal Emission and Reflection Radiometer
EVI	Enhanced vegetation Index	LTS	Linear Time Series
ANN	Artificial Neural Network	UTFVI	Urban Thermal Field Variance Index
LULC	Land-Use Land-Cover	LSTM	Long Short-Term Memory
GWR	Geographically Weighted Regression	RNN	Recurrent Neural Network
TIRS	Thermal Infrared Sensor	OLI	Operational Land Imager
VIF	Variance Inflation Factor	USGS	United States Geological Survey
TOA	Top of Atmosphere	BT	Brightness Temperature
MAPE	Mean Absolute Percentage Error	MAE	Absolute Percentage Error
MSE	Mean Squared Error		

1. Introduction

Urbanization has substantially influenced the Earth's environment over time (Qu and Long, 2018). Moreover, urbanization can significantly impact the local weather and climate. Changes in the immediate environment due to urbanization cause an increase in the warmth of metropolitan areas relative to neighbouring countryside areas, which is a straightforward demonstration of ecological deterioration. The surge in inhabitants of metropolitan areas, with the associated enlargement of the economy, has resulted in the massive development of urban areas (G. Chen et al., 2023; X. Chen et al., 2023). For example, the Sialkot district in the Punjab province of Pakistan is experiencing rapid urbanization and development. The reason for this swift expansion is that the city is an industrial hub contributing significantly to countries' annual exports and national exchequers, thus offering employment and attracting job-seekers (Kumar et al., 2024a,b).

The urbanization process results in surface and atmospheric transformations, which normally ensure changes in the thermal environment of metropolises hotter than the adjacent rural areas. This is characterized by the Urban Heat Island (UHI) effect (Srivanit et al., 2012). Most metropolises are experiencing UHI due to urbanization (Hou et al., 2019). Several studies have documented that elevated energy and water intake are associated with the UHI effect. During the summer season, the UHI significantly influences the surge in energy requirement, and this increase in energy requirement is primarily due to air conditioning systems (Fu and Weng, 2016).

In addition to the increase in electricity utilization and temperature, UHI also results in intensified pollutant intensity over urban zones (Chen et al., 2024; Ge et al., 2024), and it affects the regional climatology by varying regional wind patterns, intensifying humidity, establishing fog and clouds, and altering the rainfall frequency. Warmer air also affects the extent of smog (ozone) formation, which is the foremost environmental and health issue. These diseases cause many deaths annually, triggered as an effect of UHI (Srivanit et al., 2012). Consequently, the pattern and extent of UHI effects have been among the critical interests of numerous urban climatology studies (Gong et al., 2024).

The UHI effect, when examined using LST, is referred to as the SUHI effect (Li et al., 2023). LST is among the major factors regulating the Earth's biological, chemical, and physical development, and is crucial for analyzing the urban environment (Lizhou et al., 2024). LST can be ascertained using the effective radiating temperature of the Earth's

surface and regulates the water and heat exchange of the Earth's surface with the atmosphere. LST has been observed to fluctuate in response to the nature of the Earth's surface and is a vital factor for several meteorological investigations, including investigations of SUHI effects (Qiu et al., 2023).

SUHI investigations have primarily focused on assessing the association between the magnitude of urbanization and LST (Sheng et al., 2017). Urbanization results in the loss of vegetation cover, thus increasing surface temperature (Qiao et al., 2019). As cities expand, the natural landscape of cities, consisting of vegetation cover or bare ground, is generally transformed into urban surfaces or even changed into different vegetation covers. Due to urbanization, the energy contact between altered land surfaces and the atmosphere causes a surge in LST, regulated by surface heat fluxes (Sun et al., 2024; Yin et al., 2023a). Several studies have investigated and documented the correlation between LST, vegetation cover, and built-up areas (impervious surfaces) (Deilami et al., 2018). For example, the spectral indices of the Normalized Difference Vegetation Index (NDVI) and percentage impervious surface area (%ISA) have also been used to study their relationship with LST (Zhao et al., 2024; Zhou et al., 2022). The authors established that %ISA is a legitimate indicator of SUHI effects and discovered a solid straight connection between %ISA and LST. The vegetation cover on the Earth's surface essentially controls climatic change rather than swift climate change related to climate sources in an area (Rivera et al., 2017). With an increase in vegetation cover, the radiative temperature noted by a sensor closely approaches the temperatures of leaves, and LST is the canopy temperature at the whole canopy cover or extreme spectral vegetation (Tomlinson et al., 2012). The impact of vegetation outline on metropolitan LST appears as boundary effects, and it is not only the vegetation cover that determines the value of LST but also the adjacent environment (Zhou et al., 2023; Zhou and Liu, 2022).

Moreover, satellite data are widely utilized to analyze and study the SUHI effect by obtaining LST (Asif et al., 2023a). For example, Mathew et al. (2016) utilized data from the Thematic Mapper and Enhanced Thematic Mapper Plus to analyze the association between vegetation indices and LST. The authors documented a robust positive correlation between the LST, NDBI, and %ISA. In contrast, the correlation between the LST and NDVI was weak. Moderate Resolution Imaging Spectroradiometer (MODIS) sensor has also been used to obtain LST and examine its relationship with NDVI, Enhanced Vegetation Index (EVI), Road Density (RD), NDBI, and %ISA (Sobrino et al., 2012). The authors observed a positive relationship between LST, NDBI, and %ISA, whereas the vegetation indices were negatively correlated with LST. Consequently, the authors concluded that the UHI effect strengthens in built-up areas, while vegetation weakens it (Zhao et al., 2024a,b).

Numerous Machine Learning (ML) and Deep Learning (DL) methodologies have been used by several researchers to predict LST based on LST data acquired in previous years from different satellite imageries. For example, Zhang et al. (2022) used thermal infrared data from MODIS to obtain LST, two vegetation indices from MODIS, NDVI and EVI, and Advanced Spaceborne Thermal Emission and Reflection Radiometer Digital Elevation Model (ASTER DEM) and RD as inputs. The authors developed a Linear Time Series (LTS) prediction model and found a positive link between the observed and predicted LST. Yin et al. (2023c) also used previously mentioned inputs but developed a Support Vector Regression (SVR) model to predict LST. The authors also compared the outcomes of the SVR model with an ANN model and discovered that the SVR model outperformed the ANN model (Yu and Zhou, 2024).

Li et al. (2011) assessed LULC change through SVM-supervised classification, seasonal (winter and summer) LST, and Urban Thermal Field Variance Index (UTFVI) variations from Landsat 4, 5, and 8 satellite data for 2000, 2010, and 2020. The authors successfully implemented a Cellular Automata-based ANN algorithm to forecast LULC, seasonal LST, and UTFVI 2030 for Dhaka, Bangladesh. Furthermore, the

projected UTFVI and LST showed that a significant portion of the total area would have extreme UTFVI and LST values. The correlation analysis showed that the relationship between LST and NDBI was strongly positive but strongly negative with NDVI (Asif et al., 2023b).

DL techniques such as CNN have recently attracted considerable interest due to their outstanding feature recognition and prediction modeling performance. Montaner-Fernández et al. (2020) used a CNN model to assess the Subsurface Temperature (ST) in the Pacific Ocean from satellite measurements, including sea surface salinity, sea surface temperature, and sea surface height. The authors used multisource sea surface parameters to establish a monthly CNN model to reconstruct ocean ST and used Argo data for accurate validation. The results showed that the CNN could accurately estimate the ST of the Pacific Ocean. Baqa et al. (2022) proposed a time-series projection scheme of LST using cloud interference to unravel the problem of the influence of the lack of data on LST prediction. LST's temporal and spatial tendencies and different LULC indices were analyzed using Landsat 7 and 8 data from 2010 to 2019 for Beijing. The Geographically Weighted Regression (GWR) process simulated the LST centred on the current period. A DL prediction system based on convolution and Long Short-Term Memory (LSTM) networks was erected to predict the spatial dissemination of LST during the following observation period. The LST modeling findings showed that the estimation accuracy using the GWR method on water bodies and watertight surfaces was superior to the vegetation area. The results showed that the spatial pattern of the LST prediction using DL was relatively good.

Using the same inputs as Tariq et al. (2020), used a DL model, namely CNN, to predict LST for the Lahore District, Punjab, Pakistan. The authors also compared the accuracy of the developed model with that of other DL models, specifically ResNet, GoogLeNet, and VGGNet. Moreover, the authors found that the CNN model was the best. After successfully implementing the CNN model and various other CNN architectures, Tariq and Shu (2020) attempted to implement another prominent DL algorithm, the Recurrent Neural Network (RNN). The RNN architecture and LSTM were used for the same objective. The authors compared the performance of LSTM with ANN and observed that the LSTM model outperformed the ANN model.

As industries are a good source of attraction owing to job opportunities, they have brought many migrants from other areas of Pakistan to Sialkot. This made them seek a permanent settlement in the area, causing the expansion of urban areas and converting agricultural land to built-up land (Farhan et al., 2024; Tufail et al., 2024).

From 1990 to 2018, the built-up area of Sialkot City increased from 28.89% to 74.56%. However, the agricultural area has reduced from 69.5% to 24.84%. In addition, the saturation value has declined from 0.85 to 0.75, indicating that the city is moving towards urban sprawl (Tariq et al., 2021b).

The district has become highly susceptible to environmental pollution owing to swift urbanization, industrialization, and agricultural development. The surface and groundwater of the area have been endangered owing to rapid industrialization (Liu et al., 2023). Considering the potential future problems resulting from urbanization in the Sialkot District and its importance as an industrial and economically promising area, it is important to consider this area for LST and SUHI analysis and underline the spatial patterns there so that better courses of action can be adopted to make the area sustainable.

Consequently, the current research aims to build a DL model, namely a CNN, to predict different spectral indices and the LST and evaluate the SUHI effect for the Sialkot district. As the district lacks a study in which the relationship between LST and spectral indices has been established, future trends are projected. Given the state of the current development in the district, it is essential to carry out such a study to pinpoint the relationship between the LULC change caused by urbanization and the LST and offer the results for city planners. Thus, the outcomes of this study will offer valuable insights for planners and decision-makers in aligning the development of cities with sustainable development.

2. Study area

The district lies between $32^{\circ} 31' 12''$ N and $74^{\circ} 33' 00''$ E. A map of the study area is shown in Fig. 1. The Sialkot district is in the province of Punjab and is situated east of Pakistan beside the river Chenab. The study area, Sialkot district, falls under the Köppen climate classification "Cwa," which denotes a humid subtropical climate with dry winters and hot summers. This classification is characterized by significant seasonal variations in temperature and precipitation. Summers are typically hot and humid, with temperatures often exceeding 35°C , while winters are mild and dry, with average temperatures ranging from 10°C to 20°C (Tariq and Shu, 2020). Climatically, it is heated and tropical through summer and cold during winter. June and July are the five months when the peak temperature exceeds 40°C . The temperature in winter temperature goes down to 4°C . The area receives rainfall loads in approximately all seasons with a significant part of the rainfall during the monsoon season (from July to August) and a mean annual rainfall of approximately 1000 mm.

Sialkot District is an industrial area with several industries. The centre of the Sialkot District is Sialkot City, which is the third most prosperous city with substantial economic significance (Shah et al., 2021). The surgical, leather, and sports industries are the most prominent in Sialkot. More than 3221 industrial units manufacture surgical instruments, leather goods, sports goods, textiles, and so on (Tariq et al., 2021a). It is recognized globally for its surgical instruments, leather products, sports goods, ceramics, and processed food (Tariq et al., 2022b). The Sialkot district is renowned for yielding the world's famed Basmati rice and cereal crops (Rehman et al., 2023).

3. Materials and methods

The present study used LST and different LULC spectral indices retrieved from Landsat-8 Operational Land Imager (OLI) and Thermal Infrared Sensor (TIRS) images. The NDVI, NDBI, Modified Normalized Difference Water Index (MNDWI), and Soil-Adjusted Vegetation Index (SAVI) were used in this study. Instead of using MODIS products, the indices were computed using Landsat-8 images because of their better resolution. The correlation coefficient between the LST and the indices was also computed to distinguish the indices with a high correlation with the LST. The purpose of establishing indices with high correlation is only to choose these indices for further processes to simplify the prediction process. The model's accuracy was also assessed by employing different statistical measures, including kappa index statistics, to check the model's performance. Moreover, impervious surfaces were extracted from the NDBI images, and the results were compared with the LST. Finally, the SUHI for the study area was computed using impervious areas and normalized LST images.

3.1. Datasets

The present study utilized daytime Landsat-8 OLI and TIRS satellite images acquired in 2013, 2015, 2017, 2019, and 2021. The data used are open-access and freely available from the United States Geological Survey (USGS) website. The attainment times of the satellite images for different years were selected based on the identical attainment calendar month, which in the present case was June, and under cloud-free conditions. Due to the reason that a single tile did not entirely cover the study area, two adjacent tiles were acquired every year. The paths and rows of the acquired satellite images were 149/037 and 149/038, respectively. The spatial resolution of the multispectral bands of Landsat-8 was 30 m, which was used to compute the spectral indices. At the same time, the thermal bands of Landsat-8 with a spatial resolution of 100 m were used to retrieve LST. Moreover, the Landsat data used were atmospherically corrected.

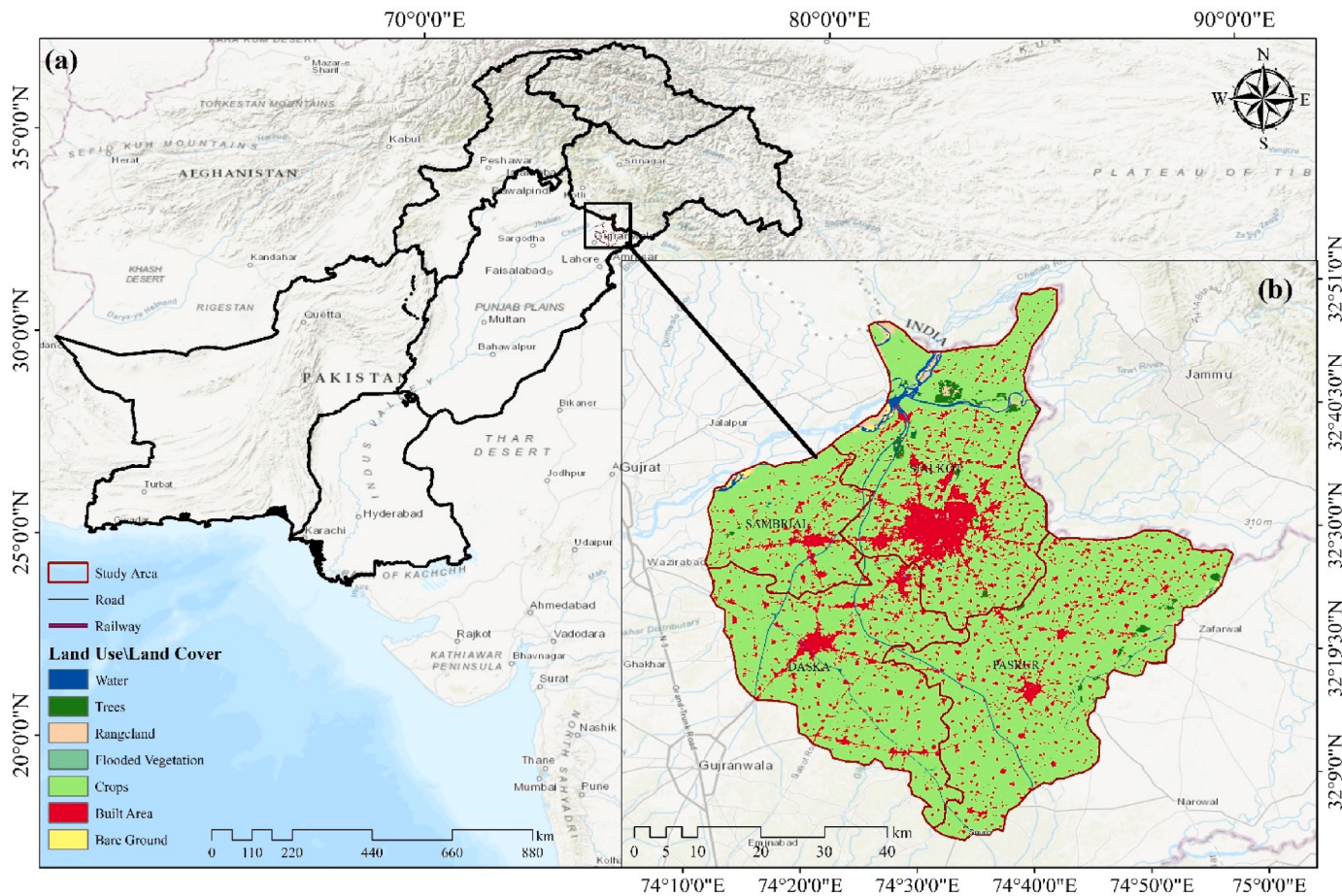


Fig. 1. (a) the Geographical location of Pakistan, (b) the geographical location of the study area.

3.2. The working framework of the study

Firstly, the Semi-Automatic Classification plugin in the QGIS software was used for the atmospheric correction of the obtained data. Secondly, the 100 m thermal band was resampled to 30 m to match the spectral indices' resolution using a common and simple resampling method called the Nearest-neighbor interpolation in the QGIS software.

To assess the possible multicollinearity between different indices the multicollinearity test was performed using Variance Inflation Factor (VIF) statistics. VIF is usually used to detect the presence of collinearity in multiple linear models (Baqi et al., 2022). By regressing each indice with others, the VIF was calculated with equation (1):

$$VIF = \frac{1}{1 - R^2} \quad (1)$$

Where R^2 represents the coefficient of determination. $VIF < 10$ means there is no multicollinearity between the indices. Whereas, $VIF > 20$ means there is serious multicollinearity between the indices. However, if $10 \leq VIF \leq 20$, there is a certain amount of autocorrelation between indices. Followingly, the correlation between LST and the spectral indices (NDVI, NDBI, MNDWI, and SAVI) was examined using the R-squared (R^2) value. The R^2 values were calculated for all of the indices and LST for the years 2013, 2015, 2017, 2019, and 2021, and then the average value was obtained. Moreover, Pearson's correlation ($\alpha: 0.05$) between the spectral indices and SUHI for the year 2021 was also determined.

Further assessments were performed between LST and the two indices, NDBI, and NDVI, due to their higher correlation with LST. The prediction of LST and the two indices was performed successively. In the

first step, the indices of 2013, 2015, and 2017 were used to model the indices for 2019. Then, in the second step, the indices of 2015 and 2017 and the predicted indices of 2019 were used to predict the indices for 2021. Finally, in the third step, the indices for 2017 and the predicted indices for 2019 and 2021 were used to predict the indices for 2023. The exact sequence was adopted to predict the LST. It is important to note that while predicting the LST for 2019, 2021, and 2023, the predicted indices of these years were used.

3.3. Used spectral indices and their extraction

Spectral indices (NDVI, SAVI, MNDWI, and NDBI), or land cover indices, are crucial for precise LST computation. In the present study, these indices were computed for 2013, 2015, 2017, 2019, and 2021. The NDVI and SAVI are key indices for examining vegetation conditions (Asif et al., 2023b; Basharat et al., 2022). NDVI is a very commonly used index, whereas SAVI was suggested as an alteration of NDVI to be appropriate for ground illumination impacts in situations with low vegetation cover. The following formulas were used to compute NDVI (J. W. Rouse, 1973) (Equation (2)) and SAVI (Huete, 1988) (Equation (3)):

$$NDVI = \frac{NIR - Red}{NIR + Red} \quad (2)$$

$$SAVI = \frac{NIR - Red}{NIR + Red + 0.5} \times 1.5 \quad (3)$$

where NIR is the near-infrared band of Landsat-8.

Furthermore, the MNDWI is essential for administering groundwater

reserves and observing water scarcity (Tariq et al., 2021a). Among the indices for urban area extraction, NDBI is the most favoured. Equations (4) and (5) were used to obtain the spectral indices of the MNDWI and NDBI as follows:

$$MNDWI = \frac{Green - MIR}{Green + MIR} \quad (4)$$

$$NDBI = \frac{SWIR1 - NIR}{SWIR1 + NIR} \quad (5)$$

where MIR is the middle infrared band and SWIR1 is the short-wave infrared 1 band of Landsat-8.

3.4. Extraction of LST

The first step in the extraction of LST is the conversion of Digital Numbers (DNs) to Top of Atmosphere (TOA) radiance (Tariq et al., 2020). Thermal infrared DNs can be converted to TOA radiance using a radiance rescaling factor. TOA radiance conversion adjusts solar illumination differences prompted by factors such as the earth-sun distance and solar elevation angle (Jamei et al., 2019a). Equation (6) is used to compute the TOA radiance.

$$L_\lambda = ML \times Q_{cal} + AL - O_i \quad (6)$$

where L_λ is the TOA radiance, ML (3.3420E-04) and AL (0.1) are the radiometric rescaling constant values for band 10 to calculate the radiance, Q_{cal} is the quantized and calibrated standard product pixel values of band 10 (DNs), and O_i (0.29) is the corrective value for band 10. These values were obtained from the metadata files.

Following the conversion of DNs to TOA radiance, TOA radiance was converted to TOA Brightness Temperature (BT) using the following equation (7) (Jamei et al., 2019b):

$$BT = \frac{K_2}{\ln\left(\frac{K_1}{L_\lambda + 1}\right)} - 273.15 \quad (7)$$

where K_1 (774.8853) and K_2 (1321.0789) are thermal constants. The values were obtained from the metadata files.

The next step in the extraction of LST involves the computation of Land Surface Emissivity (LSE). LSE is the average emissivity of an element of Earth computed from NDVI values. The LSE can be calculated from the NDVI. The NDVI was computed using the same formula as given by Equation (8), which includes using the NIR and Red bands. The LSE calculation also requires the calculation of the proportion of vegetation (P_v). Thus, P_v was computed using the following equation (8) (Sun et al., 2024):

$$P_v = \left(\frac{(NDVI - NDVI_{min})}{(NDVI_{max} - NDVI_{min})} \right)^2 \quad (8)$$

$NDVI_{min}$ and $NDVI_{max}$ were obtained from the histogram of NDVI images as the minimum and maximum, respectively. Subsequently, the LSE was computed using the following equation (9):

$$LSE = 0.004 \times P_v + 0.986 \quad (9)$$

where, 0.986 is the correction value of the equation.

Finally, LST was computed using the TOA BT, the wavelength of emitted radiance (λ), and LSE. Equation (10) (Pal and Ziaul, 2017) was used to compute the LST and was exercised as follows:

$$LST = \frac{BT}{\left(1 + \left(\frac{\lambda \times BT}{C_2} \right) \times \ln(LSE) \right)} \quad (10)$$

where, C_2 is equal to 14388 mK according to Planck's radiation formula.

3.5. Convolutional neural network (CNN)

CNN have more intricate network arrangements, more robust feature understanding, and demonstration abilities than conventional ML methods (Qu and Long, 2018). An individual neuron was handled as a filter, slid as its responsive field, and local data were evaluated using a filter. On the output of the convolutional layer, a nonlinear mapping process was accomplished using the layer of Tanh. The successive convolutional layers sandwich the pooled layer, which is operated to reduce the number of constraints and data, thereby decreasing overfitting. Generally, a fully connected layer is presented at the end of the CNN, which is identical to the context of neurons in conventional neural networks (Qu and Long, 2018).

The pertinency of CNN relies on the capacity to distribute weights; therefore, the expansion of parameters does not limit the network depth of a CNN. Moreover, a positive CNN is in the standard convolution kernel, which effectively handles data featuring high dimensions and can necessarily obtain certain superior features, increasing the pace of feature organization (Srivanit et al., 2012), which can augment the correctness of prediction. Accordingly, this study proposes employing a CNN to structure the prediction model using data from previous years.

3.5.1. Experimental Setup of CNN

The network structure of the CNN is shown in Fig. 2. The structure comprises a 4-layer convolution operation tailed by three fully connected layer operations. The filter size of the first convolutional layer was 5×2 and the stride was (5,1). In other words, the features of the two data points are augmented by the parallel features of the filter, and the total is obtained. Following the estimation of one block area, the stipulated stride (5,1) moves to other places until a 2D matrix (45 × 36) is swathed. Next to the 4-layer convolution operation, the data dimension was tiled into 1D data, input to the fully connected layer, and later subjected to a 3-layer neural network operation. Ultimately, the output was obtained in 18 layers of the predicted values.

Fig. 3 illustrates the prediction process of the LST/indices by forming a CNN model from the remote sensing observation data used in this study. First, a training dataset is constructed. Training features were randomly chosen from the original satellite data. The extracted LST/indices from the satellite data were used as testing markers, and all datasets were standardized. The training data are handled as a 2D image that operates as a convolution operation for the confined view field. A single convolution unit drives the features of each data point.

Second, the CNN model was trained, and the best possible model was achieved by altering the parameters (see Table 1). Adagrad optimization and Tanh activation functions were used. The parameter settings of the CNN model and their corresponding descriptions are listed in Table 2. The optimal arrangement of the convolutional, pooled, and fully connected layers was determined by scrutinizing each RMSE. The training data (Landsat-8 satellite data) were used as input data for the training process, whereas the extracted LST/indices were used as training markers.

3.5.2. Error estimation of the obtained and modelled LST and indices

The statistical measures utilized to assess the functioning of the proposed CNN model in this study were the Mean Absolute Error (MAE), Mean Absolute Percentage Error (MAPE), and Mean Squared Error (MSE). The model-predicted LST/indices were compared with the extracted LST/indices and the error was computed. The Absolute Error (E_A), given by equation (11) (Lam et al., 2001), in the model's prediction of LST indices, was computed by obtaining the remainder for every pixel value between the extracted and predicted LST indices.

$$E_A = |X - Y| \quad (11)$$

where X and Y are the extracted and predicted values of the LST indices for a pixel, respectively. MAE was calculated by taking the mean E_A of

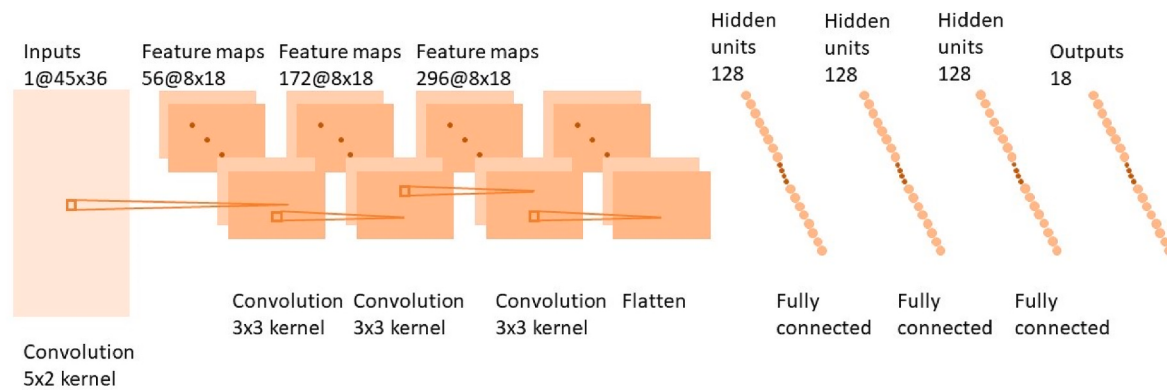


Fig. 2. The structure of the CNN model used in this study.

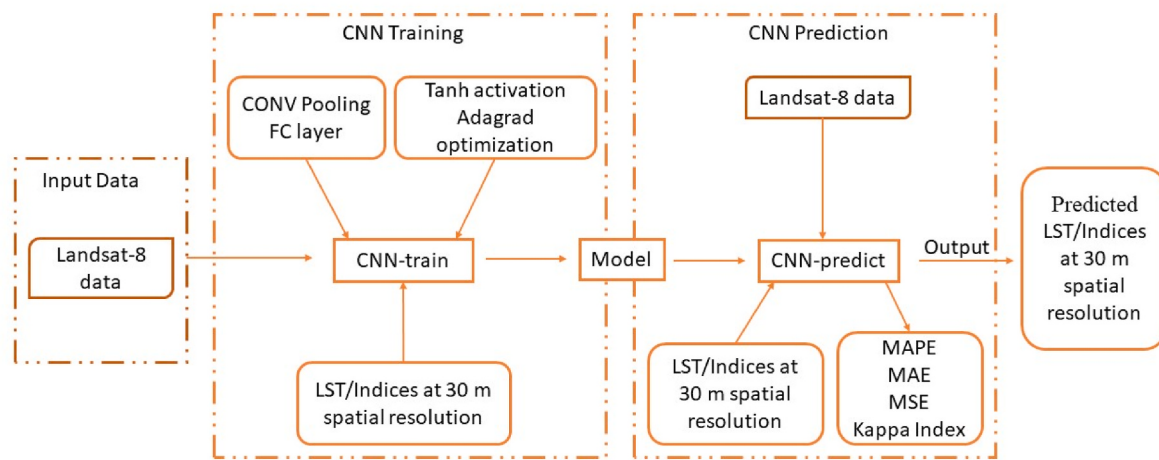


Fig. 3. Flow chart for predicting the LST and indices by the CNN model using the Landsat-8 data (30 m spatial resolution).

Table 1
Correlation statistics for the indices.

Indice	R ²	Pearson's r	VIF
SAVI	0.69	-0.65	3.95
MNDWI	0.76	-0.53	4.42
NDBI	0.93	0.75	4.65
NDVI	0.89	0.71	3.98

Table 2
Parameter settings of the CNN model.

Parameters	Setting values	Description
Convolutional kernels	3	These kernels extract low-level representations
Fully connected units	3	These neurons contain high-level features
Epoch	30	Number of cycles that the network makes through the entire training set
Optimizer	Adagrad	Updates the network parameters to curtail the loss function value
Loss function	Root mean square error function	Measures the affinity among the prediction and actual label
Activation function	Tanh	Converts linear relationships into nonlinear ones
Learning rate	0.003	The speed of network convergence

every pixel with equation (12) (Chai and Draxler, 2014).

$$MAE = \frac{\sum E_A}{n} \quad (12)$$

where E_A is the absolute error of the individual pixels and n is the total number of pixels. The Percentage Error (PE) was computed by dividing E_A of an individual pixel by its corresponding X value by equation (13) (Srivanit et al., 2012).

$$PE = \frac{E_A}{X} \quad (13)$$

MAPE was calculated by taking the mean of the PE of every pixel with equation (14) (Khatakho et al., 2021).

$$MAPE = \frac{\sum PE}{n} \quad (14)$$

where PE is the percentage error of individual pixels and n is the total number of pixels. The MSE was computed using the following formula in equation (15)(Chai and Draxler, 2014).

$$MSE = \frac{\sum (X - Y)^2}{n} \quad (15)$$

where X and Y are the extracted and predicted values of the LST/indices of the individual pixels, respectively, and n is the total number of pixels.

3.5.3. Performance evaluation of obtained and predicted LST and indices

The LST maps obtained and predicted for 2019 and 2021 were compared to evaluate the performance of the CNN model. The kappa

index was used for comparison. The standard kappa index supports the establishment of a legitimate model (Basharat et al., 2022). The Kappa index offers insights into the rational dynamics of the potency or impotence of outcomes (Wahla et al., 2022). The kappa index was computed in terms of statistics including K_{standard} , K_{location} , $K_{\text{locationsStrata}}$, and K_{no} . K_{standard} is the standard kappa index of agreement, K_{location} is the kappa for grid-cell level location, $K_{\text{locationsstrata}}$ is the kappa for

stratum-level location, and K_{no} is the kappa for no information. The probable values of the kappa index vary from 0 to 1, where 1 signifies excellent agreement and 0 indicates no agreement. These values are centred on a comparison at the pixel level of the reference and modelled data.

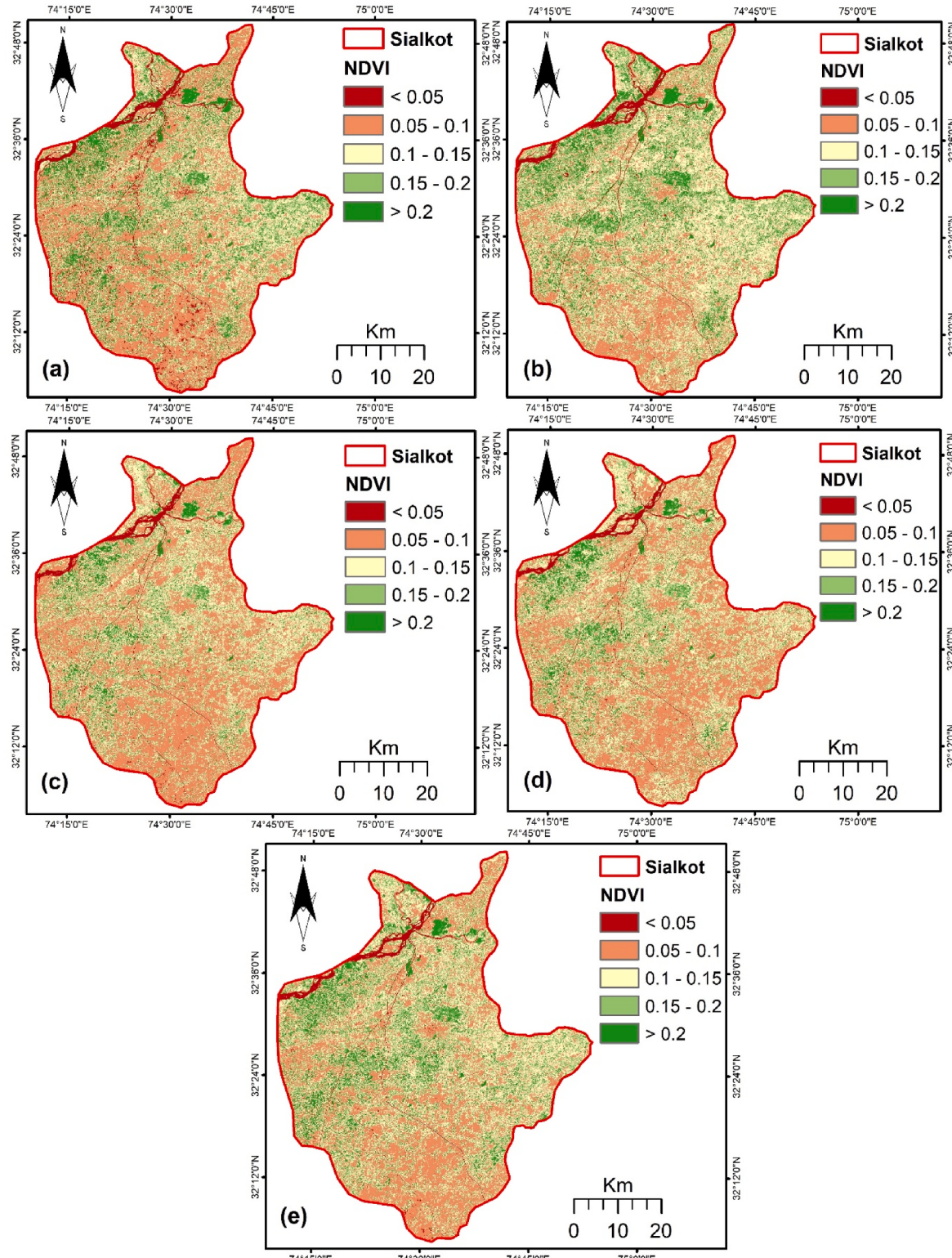


Fig. 4. Extracted NDVI of the study area for 2013 (a), 2015 (b), 2017 (c), 2019 (d), and 2021 (e).

3.5.4. Impervious area and SUHI extraction

As mentioned previously, NDBI is one of the most correlated indices with LST and is also among the essential indices for acquiring urban details such as impermeable areas. NDBI describes a single-band grey-level illustration that demonstrates urban components instead of detaching non-urban and urban categories, as in the case of an illustration of a binary image. Thus, to acquire a regional layer of impervious areas from NDBI, it is necessary to establish an optimum limiting rate and apply it to isolate non-impervious and impervious surfaces. Otsu's thresholding technique is among the most frequently applied techniques for developing a limiting value for grayscale images (Tariq et al., 2022b). Jamei, Rajagopalan, and Sun (2019a) implemented the same technique for the extraction of SUHI and achieved very convincing results. So, this study has followed the same implementation as adopted by Jamei, Rajagopalan, and Sun (2019a).

This technique establishes the optimum limiting value centred on discriminant analysis. This technique amplifies the variance among classes of the grey-level histogram to ideally split the categories. The impervious areas for both the obtained (2021) and predicted (2021 and 2023) NDBI indices were obtained using Otsu's thresholding method. Similar to the extraction of impervious areas, the obtained LST for 2021 and the predicted LST for 2021 and 2023 were normalized; therefore, SUHI dissemination was extracted. To analyze the spatial distribution of LST with LULC, it was necessary to normalize LST. When comparing various data sets or collection periods of two or more satellite images, normalizing decreases the temporal inconsistency of atmospheric conditions.

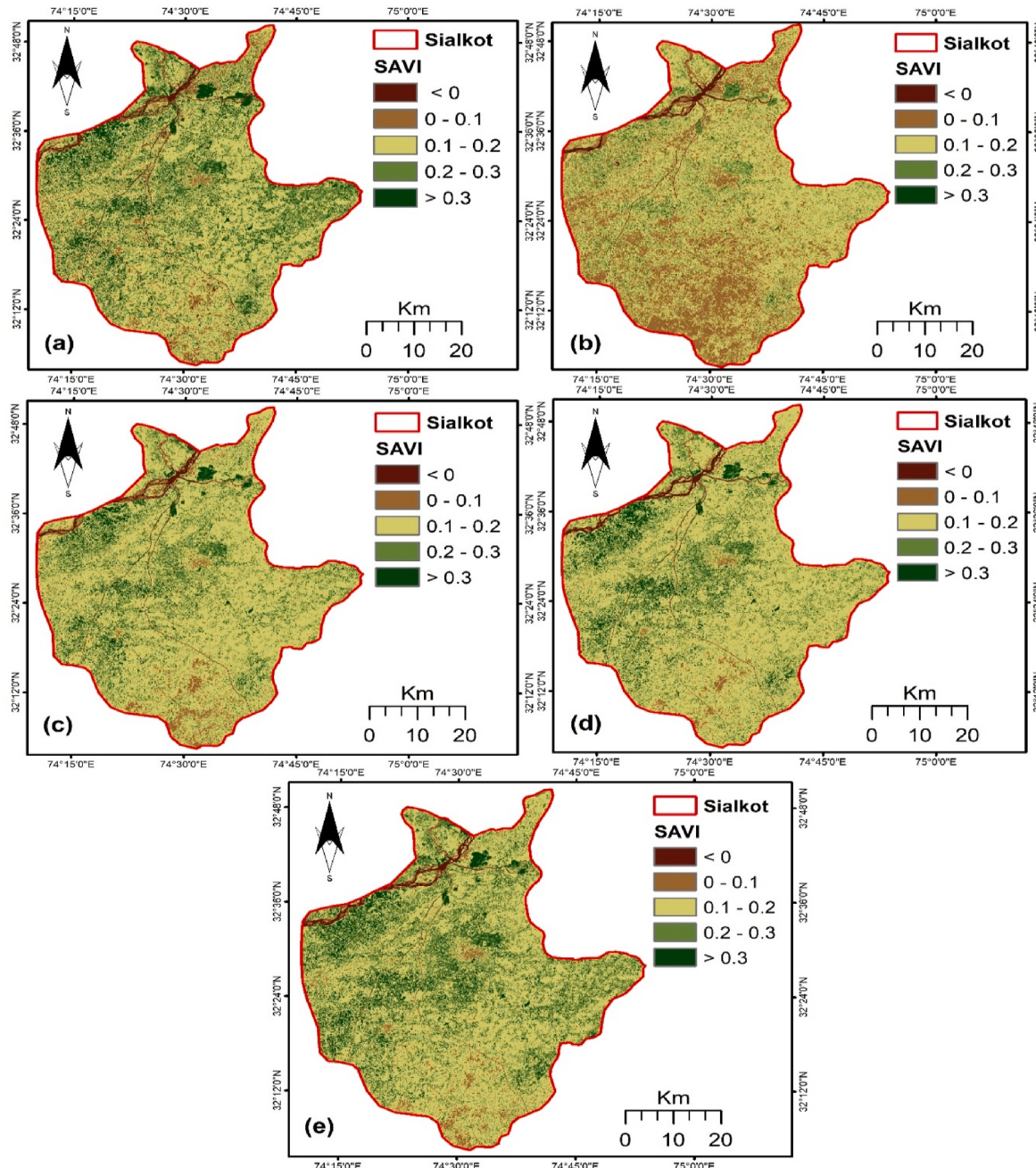


Fig. 5. Extracted SAVI of the study area for 2013 (a), 2015 (b), 2017 (c), 2019 (d), and 2021 (e).

4. Results

4.1. Obtained spectral indices and LST for 2013, 2015, 2017, 2019, and 2021

The spectral indices, namely NDVI, SAVI, NDBI, and NDWI, were obtained for 2015, 2017, 2019, and 2021, and are shown in Figs. 4–7. The LST values for 2013, 2015, 2017, 2019, and 2021 are shown in Fig. 8. As mentioned earlier, after obtaining the LST and all the spectral indices, a correlation analysis was carried out to identify which spectral indices had the most significant correlation with LST.

The SAVI has a VIF value of 3.95 whereas MNDWI has a VIF value of 4.42. However, the VIF value for NDBI was 4.65 and for NDVI it was

3.98. These results show that none of the indices have multicollinearity as their VIF values are less than 5. Moreover, the R^2 outcome showed that NDBI and NDVI were significantly correlated with LST with average R^2 values of 0.93 and 0.89, respectively. However, for SAVI and NDWI the obtained average R^2 values were 0.69 and 0.76 respectively. Furthermore, the SAVI has a higher negative correlation (Pearson's r : -0.65) with SUHI than MNDWI (r : -0.53). NDBI (r : 0.75) and NDVI (r : 0.71) together explain up to 78 % of the variation in SUHI. Therefore, NDBI and NDVI were ultimately included in the remainder of the analysis and used in the LST prediction.

Modification of vegetation and bare land cover, therefore, have the potential to regulate LST and, thus, SUHI in the study area. The plant cover in the area, which is primarily centred in the middle and north

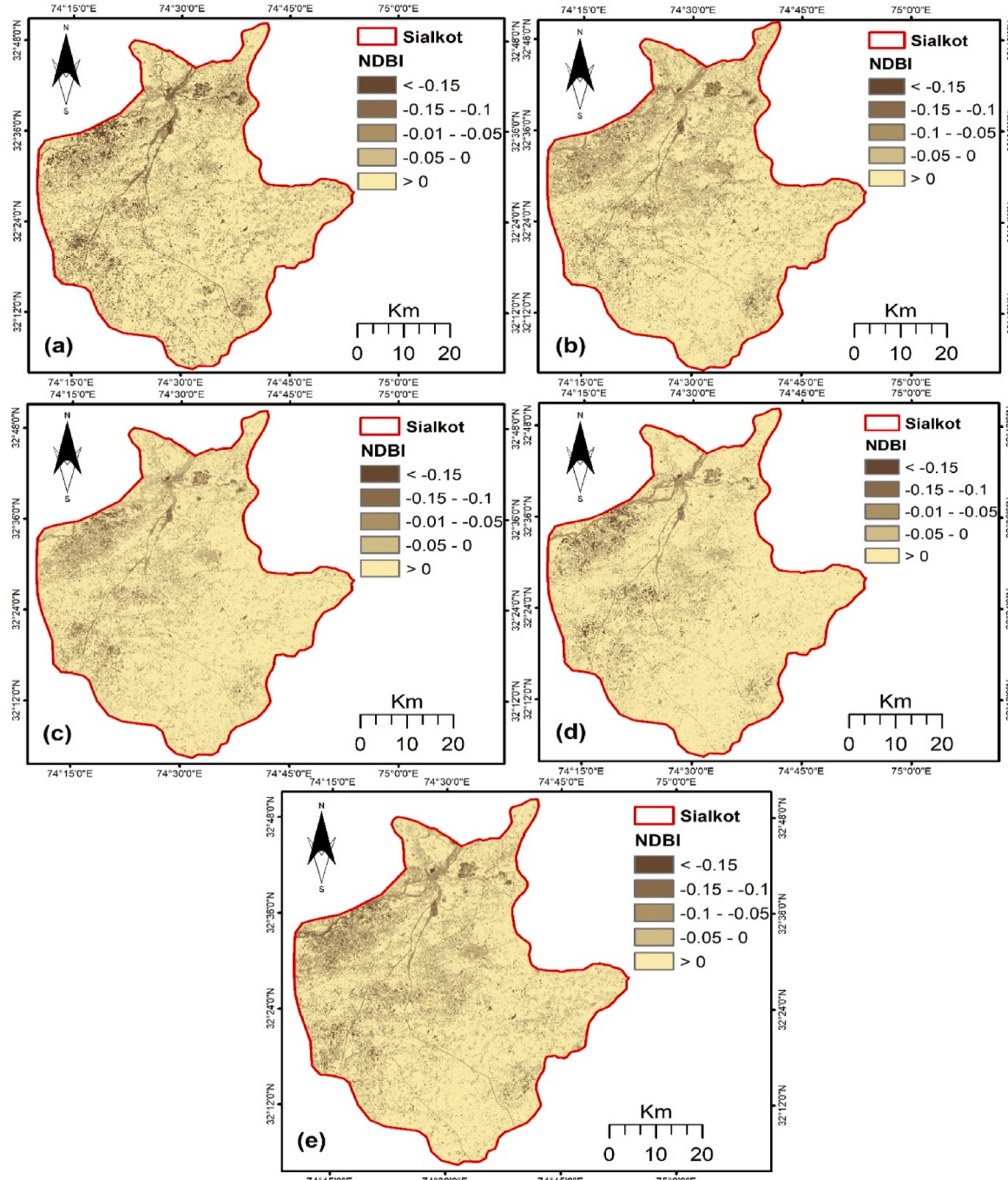


Fig. 6. Extracted NDBI of the study area for 2013 (a), 2015 (b), 2017 (c), 2019 (d), and 2021 (e).

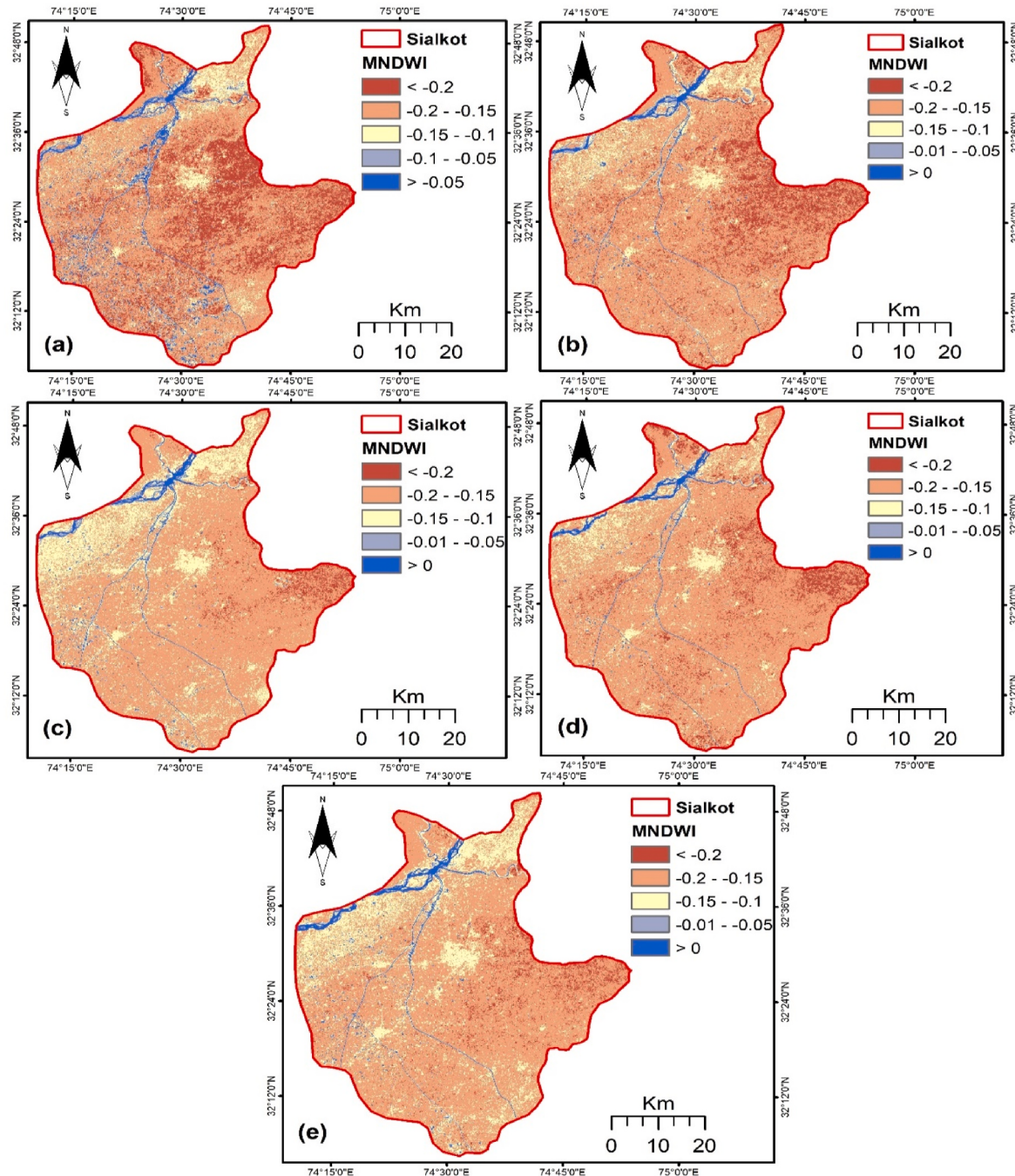


Fig. 7. Extracted MNDWI of the study area for 2013 (a), 2015 (b), 2017 (c), 2019 (d), and 2021 (e).

sides, resulted in low LST in these zones. However, the northwest and middle areas had relatively low NDBI values, resulting in higher LST in these zones. The spatial dissemination of LST in the area progressively varied from 2013 to 2021, as shown in Fig. 8. The northeastern side and the southwestern sides are the ones that are prominent and have the highest LST. In contrast, the spatial spread of LST in the extreme north, where there are water bodies, was the lowest.

In addition to the primary focus on NDVI and NDBI due to their stronger correlation with LST, the regression analysis for SAVI and MNDWI was conducted to provide a comprehensive evaluation. The R^2 values for SAVI and MNDWI were 0.69 and 0.76, respectively, indicating a moderate correlation with LST. These results, while not as strong as those for NDVI and NDBI, still contribute valuable insights into the relationship between these indices and LST. Including these findings

ensures a more thorough understanding of the data and supports the robustness of our predictive model. The manuscript will be revised to reflect these additional regression results.

4.2. Predicted spectral indices and LST for 2019, 2021 and 2023

The obtained two indices, specifically NDVI and NDBI from 2013, 2015, 2017, 2019, and 2021 were used to predict possible indices for 2019, 2021, and 2023 using the CNN model. The predicted NDVI for 2019, 2021, and 2023 are presented in Fig. 9, while the predicted NDBI for 2019, 2021, and 2023 are presented in Fig. 10. The predicted indices for 2019 and 2021 corresponded significantly to the indices obtained in these years. The predicted NDVI images showed a similar trend, where the vegetation was mainly centred on the middle and northwestern sides

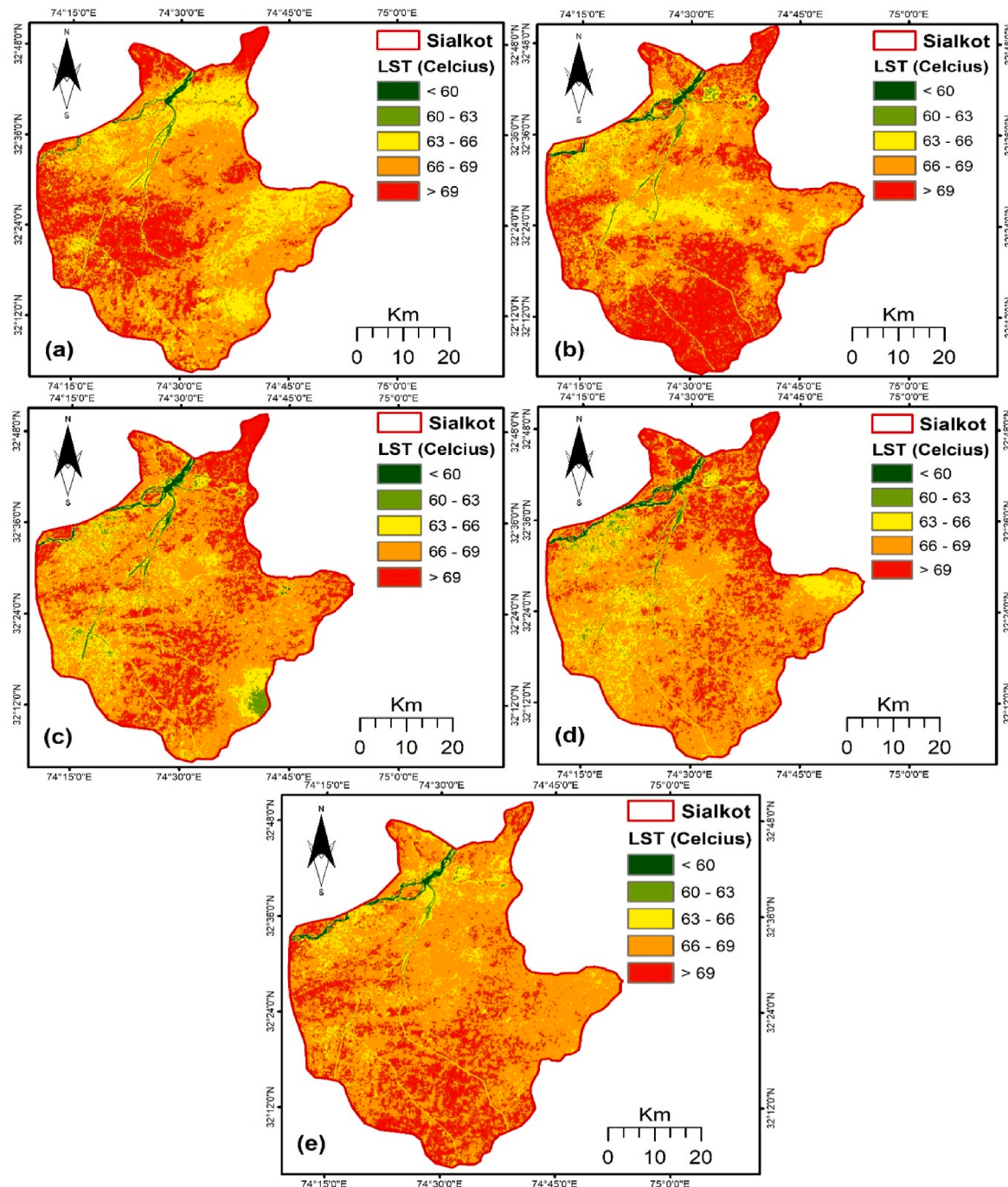


Fig. 8. Obtained LST of the study area for 2013 (a), 2015 (b), 2017 (c), 2019 (d), and 2021 (e).

of the area. Identical to NDVI, NDBI also offers a similar spatial pattern, where the southeastern side comprises primarily bare land.

Similar to the indices, the LST for 2019, 2021, and 2023 was also predicted using the LST from 2013, 2015, 2017, 2019, and 2021 through the CNN model. The predicted LST for 2019, 2021, and 2023 are shown in Fig. 11. The spatial distribution of the predicted LST for 2019 and 2021 greatly resembled the LST obtained in these years. For the predicted LST in 2019, high LST clusters were found on the southeast side, while for 2021 and 2023, the clusters were mainly centred on the extreme south side of the area.

4.3. Performance evaluation

The LST and index values predicted by the CNN model were related to the obtained values, and the inaccuracies were computed. Table 3 lists the outcomes of the comparison of 2019 and 2021 obtained and predicted Maximum, Minimum, Mean, and Standard Deviation of the indices and LST values. The predicted values based on the CNN model were quite close to the real values in the case of both LST and the indices.

The MAE, MAPE, and MSE for the comparison between the obtained and model-predicted LST and index values for 2019 and 2021 are listed in Table 4. Overall, the range of MAE and MAPE of the model in this study fluctuates between 0.11 K and 0.21 K and 0.14%–0.19%, correspondingly, which establishes that fairly lower variance exists between

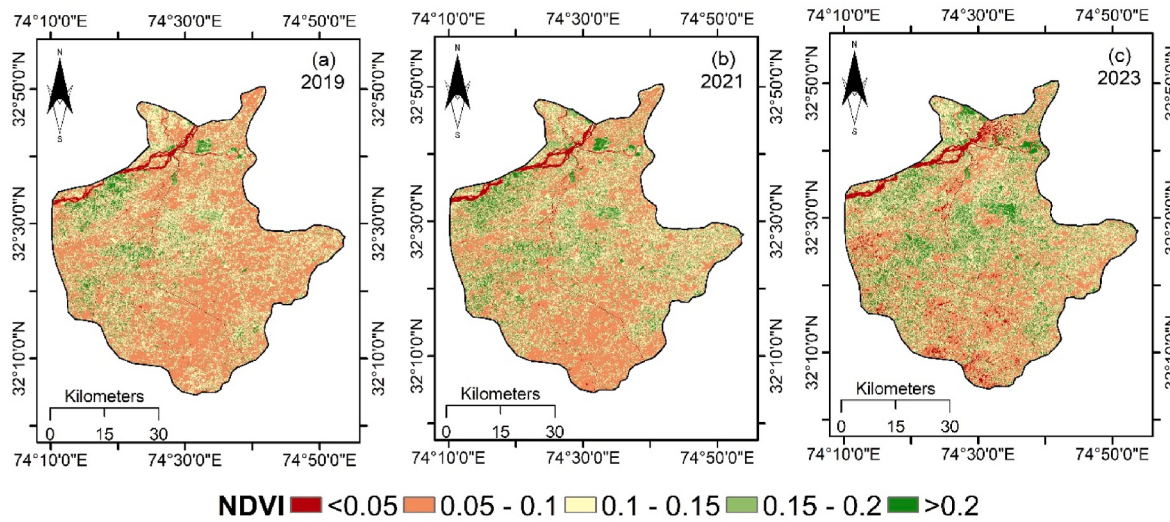


Fig. 9. Predicted NDVI of the study area.

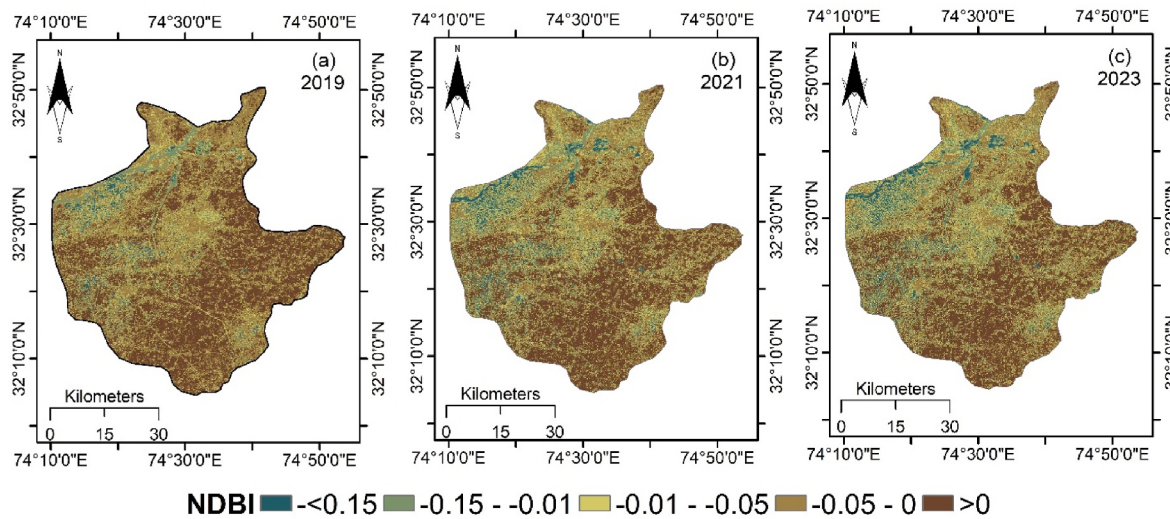


Fig. 10. Predicted NDBI of the study area.

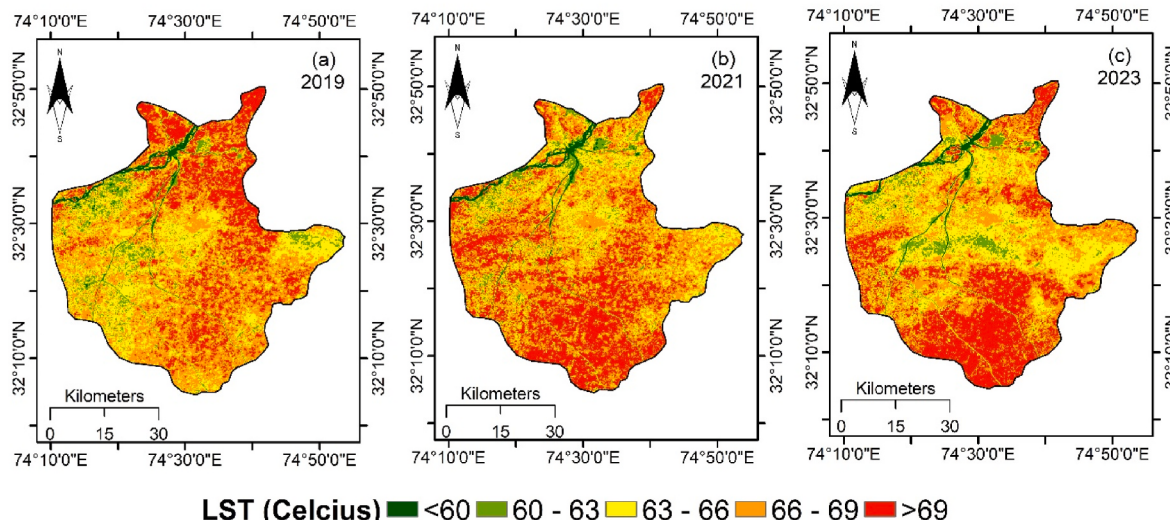


Fig. 11. Predicted LST of the study area.

Table 3

Maximum, Minimum, Mean, and Standard Deviation of obtained and predicted LST, NDVI, and NDBI for years 2019, and 2021.

Data Type	Year	Status	Maximum	Minimum	Mean	Standard Deviation
LST (°C)	2019	Obtained	74.6	53.18	66.34	1.29
		Predicted	75.13	53.98	66.79	1.18
	2021	Obtained	73.69	56.05	67.66	1.14
		Predicted	74.44	56.63	68.02	1.31
NDVI	2019	Obtained	0.41	-0.08	0.13	0.09
		Predicted	0.46	-0.07	0.15	0.11
	2021	Obtained	0.43	-0.07	0.14	0.10
		Predicted	0.44	-0.08	0.13	0.12
NDBI	2019	Obtained	0.33	-0.29	0.13	0.10
		Predicted	0.31	-0.31	0.14	0.11
	2021	Obtained	0.52	-0.33	0.18	0.08
		Predicted	0.55	-0.31	0.18	0.09

Table 4

MAE, MAPE, and MSE of LST, NDVI, and NDBI for the years 2019 and 2021.

Data Type	LST		NDVI		NDBI		
	2019	2021	2019	2021	2019	2021	
Statistical measures	MAE (K)	0.21	0.23	0.19	0.21	0.13	0.11
	MAPE (%)	0.14	0.19	0.15	0.17	0.16	0.14
	MSE	0.27	0.21	0.25	0.23	0.21	0.19

the predicted values by the CNN model and the obtained values of both LST and the indices. The value of MSE, which varies between 0.19 and 0.27 also shows excellent conformity among the predicted and obtained values of LST and the indices.

Furthermore, Table 5 shows the sum of the pixels of the LST for the research area, classified based on the prediction error of LST. A positive error implies that the value obtained is greater than the model-predicted value, whereas a negative error indicates otherwise. It can be observed from Table 5 that the CNN model was capable of predicting the LST for 2019 and 2021 for the study area very precisely, as the error in prediction for approximately 55% pixels was within 0.5 °C of the obtained LST for both years. The number of pixels for which the error is beyond 1.0 °C of the obtained LST is relatively less for the two years, and it is only 10% and 8% for 2019 and 2021, respectively, which is even less than 10% of the overall number of pixels.

The kappa index approach was used to compare the obtained and predicted LST for 2019 and 2021, and the results are listed in Table 6. The observed index for different kappa statistics, including K_{standard} , K_{no} , K_{location} , and $K_{\text{locationstrata}}$ varies from 0.83 to 0.96. Based on the threshold value of the kappa index, the model results were acceptable.

4.4. Extracted impervious area and SUHI

The predicted NDBI for 2023 and the obtained and predicted NDBI for 2021 were used to extract the impervious areas for 2021 (actual and predicted) and 2023 (predicted), as shown in Fig. 12. The impervious

Table 5

Number of pixels (% of pixels) of LST in different error ranges for the years 2019, and 2021.

Error Ranges	Between -1 and -0.5 °C	Between -0.5 and 0 °C	Between 0 and 0.5 °C	Between 0.5 and 1 °C	Between 1 and 1.5 °C
Year	2019	276451 (8%)	380120 (11%)	1555041 (45%)	1174917 (34%)
					69112 (2%)
	2021	241894 (7%)	345564 (10%)	1589597 (46%)	1244030 (36%)
					34556 (1%)

Table 6

Kappa statistics for the ability of the model to predict LST for 2019, and 2021.

Statistic	Index (2019)	Index (2021)
K_{no}	0.87	0.86
K_{location}	0.93	0.92
$K_{\text{locationstrata}}$	0.96	0.94
K_{standard}	0.83	0.81

area extracted from the predicted NDBI in 2023 demonstrates a considerable rise compared to the impervious area extracted from the 2021 NDBI, as shown in Fig. 12.

In addition to extracting impermeable areas, the normalized obtained and predicted LST for 2021 and the normalized predicted LST for 2023 were used to extract the SUHI distribution shown in Fig. 13. The SUHI distribution validated the impacts of impervious areas on the LST distribution, as shown in Fig. 13. The results revealed that the distribution of impervious areas is significantly linked to the distribution of SUHI.

5. Discussion

The current study used Landsat-8 satellite data to obtain different LULC spectral indices and LST for 2013, 2015, 2017, 2019, and 2021. The obtained data were then utilized to build a CNN model to predict the geographical distribution of the LST and indices in this study. The rapidly urbanizing and developing district of Sialkot, situated in eastern Pakistan, was chosen as the case study area for the analysis. The selected area was an industrial hub. Industries are developing by leaps and bounds and are attracting workers from adjacent regions. Migrant workers prefer to settle in the area permanently to avoid the inconvenience of travelling, thus causing the expansion of urban zones and reducing agricultural land. Therefore, this study analyzed the spatio-temporal trends of LST and LULC spectral indices NDVI, NDBI, MNDWI, and SAVI over the study area.

The CNN model predicted the LST distributions and indices for 2019, 2021, and 2023. Afterward, the impervious area and SUHI were extracted using the obtained and predicted LST and indices for 2021 and the predicted LST and indices for 2023. The first step in this approach was to determine the correlation between different indices and LST. Thus, a correlation analysis between the obtained spectral indices and the LST was conducted to reduce the number of input variables in the prediction process.

As described in the Results section, the spectral indices that demonstrated high correlations with LST were NDBI and NDVI. As a result, only MNDWI and SAVI were utilized in the prediction process. Therefore, further analysis was performed between LST and the strongly correlated indices NDBI and NDVI. The independent variables were the NDBI and NDVI indices, whereas the dependent variable was LST. The LST for 2019, 2021, and 2023 was predicted using the predicted indices.

The results of the correlation analysis revealed that NDVI had a substantially negative relationship with LST. The negative association between LST and green spaces is probably due to the water content, albedo, and emittance of vegetation. Several studies (Bera et al., 2022; Khan et al., 2018; Wunsch et al., 2021) have also reported that dense vegetation cover contributes to a solid adverse LST-NDVI correlation. However, correlation analysis showed that NDBI was significantly positively correlated with LS. This could be due to the emittance and albedo qualities of urban materials in these zones, resulting in higher levels of LST. Several other researchers have also demonstrated a positive relationship between LST and NDBI.

After establishing the indices, the CNN model was fine-tuned using the optimal parameters in Table 2 to predict the indices and the LST. First, the NDBI and NDVI indices were predicted and reclassified to the same scale as the obtained indices. Preparations were made in succession. First, a prediction was made for 2019 using the indices obtained for

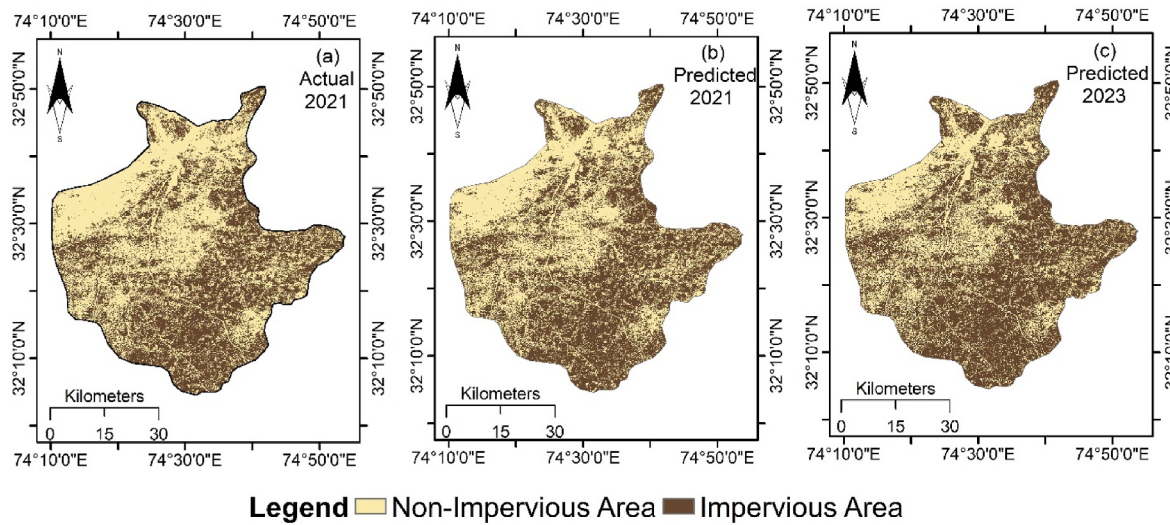


Fig. 12. Actual and predicted impervious area of the study area.

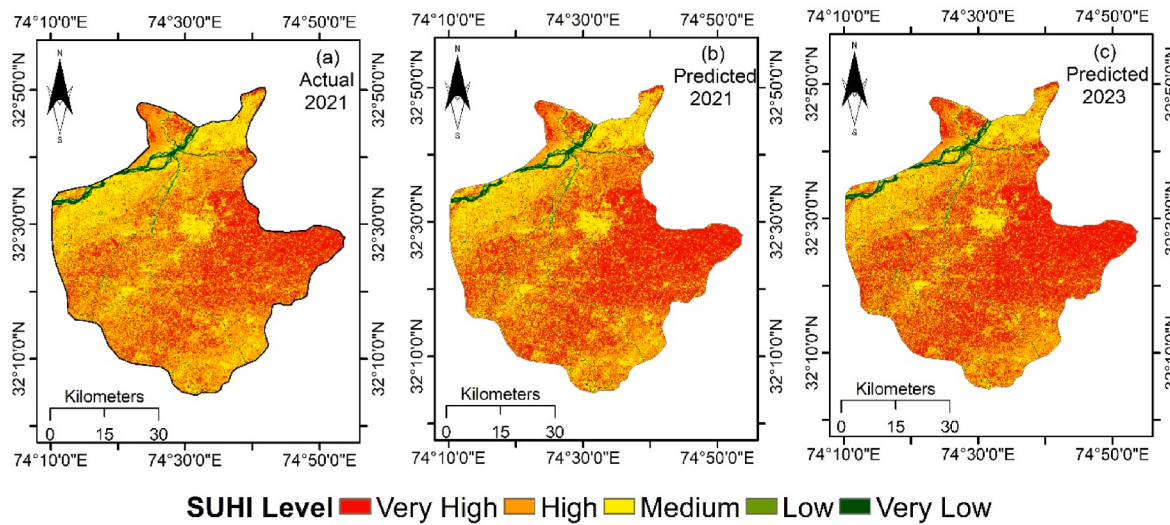


Fig. 13. Actual and predicted SUHI distribution of the study area.

2013, 2015, and 2017. Second, the predicted indices for 2019 and those obtained for 2015 and 2017 were used to predict 2021. After obtaining the prediction results for 2021, the index predictions were made for 2023. The predicted indices are shown in Figs. 9 and 10, respectively. Both high NDVI and NDBI were spatially distributed throughout the area.

Using the same approach, the CNN model was used to predict LST for 2019, 2021, and 2023. Fig. 11 shows the simulated LST for 2019, 2021, and 2023. The predicted LST for 2019 and 2021 showed a similar spatial trend to the LST obtained for 2019 and 2021. In 2019, the high LST was centred on the northeastern side of the area, whereas in 2021 and 2023, the clustering was on the southwestern side. This spatial variation can be attributed to variations in agricultural fields, temperature, and climate. The acquisition month of the satellite data for the different years in this study was June, a month of harvest and cultivation. Thus, considering June as a target month will help minimize the seasonal variation in vegetation cover on the LST.

During June, the Rabi crops, most notably wheat and barley, in the study area are almost wholly harvested, and the agricultural fields are left with only crop residue. Bare fields result in higher surface temperatures, as they are directly exposed to the scorching sun during the

hottest month of June. However, at the same time, the fields are prepared for sowing the ‘Kharif’ crops, primarily rice and sugarcane, which require much irrigation to provide cooling effects, thus resulting in a reduced surface temperature in the surrounding areas. Moreover, it is not easy to ascertain the exact harvest and sowing timing, as it varies almost yearly depending on the weather and farmer satisfaction. Consequently, this variation is a possible reason for the spatial dissemination of the LST throughout the study area.

As previously stated in the methodology section, the performance of the CNN model was evaluated by comparing the obtained and predicted LST and indices for 2019 and 2021. The cross-validation approach demonstrated that the maximum, minimum, mean, and standard deviation values of the predicted and obtained LST and indices for 2019 and 2021 were relatively close, as shown in Table 3.

Several studies (Bera et al., 2022) have used cross-validation of the Landsat and MODIS datasets. Fatemi and Narangifard (2019) cross-validated their results and correspondingly yielded RMSEs of 2.27 °C and 1.83 °C. This study used Landsat-8 derived LST and indices as reference sources to compare the predicted LST and indices. The cross-validation outcomes of the present work showed that the MSE for LST and indices range from 0.19 °C to 0.27 °C, which specifies that the

error was less than the previously conducted studies. However, previous studies (Wunsch et al., 2021; Yin et al., 2023) used MODIS LST to compare model predictions based on certain factors.

Khan et al. (2018) used the SVR model to predict LST using previous years' LST, EVI, RD, and DEM data. The SVM predicted LST, and the MODIS LST comparison indicated that the MAE and MAPE ranged from 0.521 K to 0.525 K and 0.181–0.187%, respectively. Mathew, Wunsch et al. (2021) also used the same approach as mentioned previously, except that the LTS model was the LTS model, and the study area was different. A contrast of the LST predicted by LTS and the LST obtained from MODIS showed that the MAE and MAPE fluctuate between 0.23 K and 0.31 K and 0.08 %–0.10 %, correspondingly. Basharat et al. (2022) also employed a similar approach but used a DL technique of CNN. The comparison among the CNN model predicted and MODIS LST data demonstrated that MAE changes between 0.25 k and 0.29 k, and the MAPE ranges from 0.13% to 0.15%. The results of these studies are similar to those of the present study. Hence, the CNN model can predict LST to assess the SUHI effect.

Moreover, in the present study, more than 55% of the CNN model predicted LST pixels had an error of between ± 0.5 °C of the obtained LST for 2019 and 2020. Very few pixels had an error of more than 1 °C. The contrast reveals that the predicted LST was based on the LST obtained for many pixels, as shown in Table 5. Furthermore, the obtained and CNN model predicted LST for 2019 and 2021 were compared, yielding standard kappa statistic index values ranging from 0.81 to 0.96, suggesting suitable predictions. Akhtarmash et al. (2024) conducted a multiple regression analysis to predict LST and found that the kappa index of different kappa statistics ranged from 0.73 to 0.96. These results demonstrate that the CNN model can account for LST variations across the research area.

Consequently, from the evaluation of the CNN model results, it is evident that the CNN model predicted the LST and the index values approximated the obtained values closely. Hence, the CNN model can be utilized to precisely predict LST and spectral indices. Thus, the model can be used to analyze the SUHI effects in an urban area.

Finally, the actual impervious area in 2021 and predicted impervious area in 2021 and 2023 were extracted using the observed and predicted NDBI using Otsu's thresholding approach. Subsequently, for the SUHI analysis, in addition to the actual LST in 2021, the predicted LST distributions for 2021 and 2023 were normalized to extract SUHI trends over the study area. The findings demonstrated that if the current level of urbanization and development in the research region persists, the impervious area in 2023 will be substantially more than that in 2021. A comparison of the actual results for 2021 and the predicted results for 2023 of the impervious area and the SUHI distribution shows that these two have a proportional influence; thus, the rise in SUHI depends on the impervious area.

Previously, (Naqvi et al., 2024; Tariq et al., 2023a) examined the temporal patterns of SUHIs in 31 major Chinese cities from 2001 to 2015 using MODIS LST data and China's LUCL datasets. The authors asserted that the severity of SUHI in metropolitan regions rose dramatically across most cities throughout the summer. Tariq et al. (2022a) investigated the interannual fluctuations in SUHI concentrations in 31 Chinese metropolises based on MODIS LST from 2001 to 2015. The authors concluded that the primary variables contributing to increasing SUHI levels during summer days and nights were shrinking vegetation and a growing population.

Furthermore, for Babol City in Iran, Tariq et al. (2021b) analyzed the spatiotemporal patterns of LULC variations and heat island intensity from 1985 to 2015. The authors noticed a drastic increase in urbanization and heat island concentration (SUHI intensity). The results of all the previously discussed investigations conducted at different places confirm the outcomes of the present study, indicating that urbanization and its spread considerably impact SUHI concentration. Qiao et al. (2019) recently employed MODIS LST and EVI data from 2001 to 2017 to examine the international link between SUHI and EVI intensities. The

key results of their findings revealed that the average annual nighttime and daytime SUHI concentrations amplified considerably in metropolises, and the daytime SUHI concentration was considerably linked to countryside EVI during the growth period in 58.9% of metropolises, as the elevated countryside EVI augmented the EVI distinction between rural and urban areas.

Hence, these studies also show a strong relationship between urbanization (impervious area) and SUHI. They also asserted that reducing open green spaces and transforming agricultural land into built-up land increases city temperature levels. Consequently, the continuous surge in development and urbanization in the study area will substantially increase LST and, thus, the SUHI distribution. Unfortunately, the situation is heading towards a worse future unless local authorities adopt an appropriate urban planning model.

A disadvantage of CNN is its slow parameter update, which requires considerable time to tweak the parameters and the network layer as per the investigational observations. The pooling layer is frequently combined to reduce the data dimension, leading to a shortfall in the significant information. A CNN continually stimulates a slight variety of computational data, disregarding the association between the part and the whole. The developed model is a valuable tool for predicting LST. The predicted LST could then be used to study the SUHI effect over any given area. However, new factors, such as topographic maps and other spectral indices, can be investigated in subsequent research to improve the LST analysis. In addition, the effectiveness of various modeling methods, including different ML and advanced DL methods, may be explored to provide a clear perspective on LST predictions.

6. Conclusion

This study analyzed the expected upcoming SUHI patterns centred on the growth of urban regions, considering a rapidly urbanizing and industrializing Sialkot district as a case study area, thus adding to the current SUHI analyses. To carry out the SUHI analysis, generally used functional spectral indices, such as NDBI, NDVI, MNDWI, and SAVI, were employed in this work. These indices provide relevant data on distinct land cover types. The indices and LST for 2013, 2015, 2017, 2019, and 2021 were obtained from Landsat-8 images, and a correlation analysis was used to determine the indices significantly correlated with LST.

The results revealed that the most critical indices linked with LST were NDVI and NDBI, with corresponding R^2 values of 0.93 and 0.91. Similarly, Parson's correlation analysis also showed that NDBI ($r: 0.75$) and NDVI ($r: 0.71$) positively related to the SUHI for 2021. Hence, the two indices were used in the modeling process. A CNN-based prediction process was used to predict LST and indices for 2019, 2021, and 2023. It is essential to validate the results of the proposed methodology; thus, the obtained LST and indices were utilized to assess the validity of the predicted LST and indices. The CNN model-based prediction results yielded MAE (ranging from 0.11 K to 0.23 K), MAPE (ranging from 0.14% to 0.19%), and MSE (ranging from 0.19 to 0.27) for predicted LST, and indices relevant to the observed LST and indices for 2019 and 2021, thus, exhibiting excellent prediction accuracy.

Moreover, the kappa statistic index results (ranging from 0.81 to 0.96) also demonstrated that the predictions were entirely accurate. Finally, using Otsu's thresholding approach, the impervious area and SUHI were extracted from the actual NDBI and LST of 2021 and predicted LST and NDBI of 2021 and 2023. A comparison of the observed and predicted impervious areas and SUHI for 2021 showed considerable resemblance. In addition, the predicted impervious area and SUHI distributions for 2023 show an increasing pattern.

6.1. Limitations of the study

Future studies can further enhance the accuracy and applicability of the CNN model by incorporating additional factors such as topographic

maps, other spectral indices, and socio-economic data. Exploring different ML and advanced DL methods, such as various CNN architectures and RNN, could provide a clearer perspective on LST predictions. Additionally, extending this research to other rapidly urbanizing regions can offer comparative insights and validate the model's effectiveness across different geographical contexts.

6.2. Implications of the study

Despite its promising results, this study has certain limitations. The CNN model's performance can be affected by the slow parameter update process, requiring considerable time to fine-tune parameters and network layers. The pooling layer used to reduce data dimensions may result in the loss of significant information. Moreover, the study's reliance on Landsat-8 data limits its temporal resolution, and integrating higher-resolution data from other sources could improve prediction accuracy. Addressing these limitations in future research will enhance the model's robustness and reliability in predicting LST and SUHI effects.

Funding

This work is sponsored in part by the Science and Technology Research Program of Chongqing Municipal Education Commission (Grant No. KJQN202303203, KJZD-M202203201), the Doctoral Fund of Chongqing Industry Polytechnic College (No. 2023GZYBSZK3-03), and the Natural Science Foundation of Chongqing, China CSTC, (Grant No. CSTB2023NSCQ-MSX0981). This research was supported by Researchers Supporting Project number (RSP2024R496), King Saud University, Riyadh, Saudi Arabia.

CRediT authorship contribution statement

Shun Fu: Writing – review & editing, Writing – original draft, Validation, Methodology, Investigation, Formal analysis, Data curation, Conceptualization. **Lufeng Wang:** Writing – review & editing, Writing – original draft, Visualization, Resources, Project administration, Methodology, Investigation, Funding acquisition, Data curation. **Umer Khalil:** Writing – review & editing, Writing – original draft, Visualization, Validation, Methodology, Investigation, Formal analysis, Data curation, Conceptualization. **Ali Hassan Cheema:** Writing – review & editing, Writing – original draft, Validation, Resources. **Israr Ullah:** Writing – review & editing, Writing – original draft, Software, Methodology, Formal analysis. **Bilal Aslam:** Writing – review & editing, Writing – original draft, Visualization, Validation, Supervision, Resources. **Aqil Tariq:** Writing – review & editing, Writing – original draft. **Muhammad Aslam:** Writing – review & editing, Writing – original draft, Funding acquisition. **Saad S. Alarifi:** Writing – review & editing, Writing – original draft, Validation.

Declaration of competing interest

The authors declare that they have no known competing financial interests or personal relationships that could have appeared to influence the work reported in this paper.

Data availability

Data will be made available on request.

Acknowledgements

This research was supported by Researchers Supporting Project number (RSP2024R496), King Saud University, Riyadh, Saudi Arabia.

References

- Akhtarmash, A., Abbasi-Moghadam, D., Sharifi, A., Yadkouri, M.H., Tariq, A., Lu, L., 2024. Road extraction from satellite images using attention-assisted UNet. *IEEE J. Sel. Top. Appl. Earth Obs. Remote Sens.* 17, 1126–1136. <https://doi.org/10.1109/JSTARS.2023.3336924>.
- Asif, M., Kazmi, J.H., Tariq, A., 2023a. Traditional ecological knowledge based indicators for monitoring rangeland conditions in Thal and Cholistan Desert, Pakistan. *Environ. Challenges* 13, 100754. <https://doi.org/10.1016/j.envc.2023.100754>.
- Asif, M., Li-Qun, Z., Zeng, Q., Atiq, M., Ahmad, K., Tariq, A., Al-Ansari, N., Blom, J., Fenske, L., Alodaini, H.A., Hatamleh, A.A., 2023b. Comprehensive genomic analysis of *Bacillus paralicheniformis* strain BP9, pan-genomic and genetic basis of biocontrol mechanism. *Comput. Struct. Biotechnol. J.* 21, 4647–4662. <https://doi.org/10.1016/j.csbj.2023.09.043>.
- Baqa, M.F., Lu, L., Chen, F., Nawaz-ul-Huda, S., Pan, L., Tariq, A., Qureshi, S., Li, B., Li, Q., 2022. Characterizing spatiotemporal variations in the urban thermal environment related to land cover changes in karachi, Pakistan, from 2000 to 2020. *Remote Sens* 14, 2164. <https://doi.org/10.3390/rs14092164>.
- Basharat, M. ul, Khan, J.A., Khalil, U., Tariq, A., Aslam, B., Li, Q., 2022. Ensuring earthquake-proof development in a swiftly developing region through neural network modeling of earthquakes using nonlinear spatial variables. *Buildings* 12, 1713. <https://doi.org/10.3390/buildings12101713>.
- Bera, D., Das Chatterjee, N., Mumtaz, F., Dinda, S., Ghosh, S., Zhao, N., Bera, S., Tariq, A., 2022. Integrated influencing mechanism of potential drivers on seasonal variability of LST in Kolkata municipal corporation, India. *Land* 11, 1461. <https://doi.org/10.3390/land11091461>.
- Chai, T., Draxler, R.R., 2014. Root mean square error (RMSE) or mean absolute error (MAE)? -Arguments against avoiding RMSE in the literature. *Geosci. Model Dev. (GMD)* 7, 1247–1250. <https://doi.org/10.5194/gmd-7-1247-2014>.
- Chen, X., Xie, D., Zhang, Z., Sharma, R.P., Chen, Q., Liu, Q., Fu, L., 2023. Compatible Biomass Model with Measurement Error Using Airborne LiDAR Data. *Remote Sens* 15, 3546. <https://doi.org/10.3390/rs15143546>.
- Chen, G., Zhang, K., Wang, S., Xia, Y., Chao, L., 2023. iHydroSlide3D v1.0: an advanced hydrological-geotechnical model for hydrological simulation and three-dimensional landslide prediction. *Geosci. Model Dev.* 16, 2915–2937. <https://doi.org/10.5194/gmd-16-2915-2023>.
- Chen, J., Zhao, Z., Yang, Y., Li, C., Yin, Y., Zhao, X., Zhao, N., Tian, J., Li, H., 2024. Metallogenetic prediction based on fractal theory and machine learning in Duobaoshan Area, Heilongjiang Province. *Ore Geol. Rev.* 168, 106030. <https://doi.org/10.1016/j.oregeorev.2024.106030>.
- Deilami, K., Kamruzzaman, M., Liu, Y., 2018. Urban heat island effect: a systematic review of spatio-temporal factors, data, methods, and mitigation measures. *Int. J. Appl. Earth Obs. Geoinf.* 67, 30–42. <https://doi.org/10.1016/j.jag.2017.12.009>.
- Farhan, M., Yang, J., Wu, T., Wang, S., Zhao, X., Tariq, A., 2024. Impact assessment of agricultural droughts on water use efficiency in different climatic regions of Punjab Province Pakistan using MODIS time series imagery. *Hydrol. Process.* 38, 1–16. <https://doi.org/10.1002/hyp.15232>.
- Fatemi, M., Narangifard, M., 2019. Monitoring LULC changes and its impact on the LST and NDVI in district 1 of shiraz city. *Arab. J. Geosci.* 12 <https://doi.org/10.1007/s12517-019-4259-6>.
- Fu, P., Wang, Q., 2016. A time series analysis of urbanization induced land use and land cover change and its impact on land surface temperature with Landsat imagery. *Remote Sens. Environ.* 175, 205–214. <https://doi.org/10.1016/j.rse.2015.12.040>.
- Ge, J., Wang, Y., Zhou, D., Gu, Z., Meng, X., 2024. Effects of urban vegetation on microclimate and building energy demand in winter: An evaluation using coupled simulations. *Sustain. Cities Soc.* 102, 105199. <https://doi.org/10.1016/j.scs.2024.105199>.
- Gong, X., Hou, Z., Wan, Y., Zhong, Y., Zhang, M., Lv, K., 2024. Multispectral and SAR Image Fusion for Multiscale Decomposition Based on Least Squares Optimization Rolling Guidance Filtering. *IEEE Trans. Geosci. Remote Sens.* 62, 1–20. <https://doi.org/10.1109/TGRS.2024.3353868>.
- Hou, H., Wang, R., Murayama, Y., 2019. Scenario-based modelling for urban sustainability focusing on changes in cropland under rapid urbanization: a case study of Hangzhou from 1990 to 2035. *Sci. Total Environ.* 661, 422–431. <https://doi.org/10.1016/j.scitotenv.2019.01.208>.
- Huete, A.R., 1988. A soil-adjusted vegetation index (SAVI). *Remote Sens. Environ.* 25, 295–309. [https://doi.org/10.1016/0034-4257\(88\)90106-X](https://doi.org/10.1016/0034-4257(88)90106-X).
- Jamei, Y., Rajagopalan, P., Sun, Q., 2019a. Spatial structure of surface urban heat island and its relationship with vegetation and built-up areas in Melbourne, Australia. *Sci. Total Environ.* 659 (Chayn), 1335–1351. <https://doi.org/10.1016/j.scitotenv.2018.12.308>.
- Jamei, Y., Rajagopalan, P., Sun, Q.C., 2019b. Time-series dataset on land surface temperature, vegetation, built up areas and other climatic factors in top 20 global cities (2000–2018). *Data Br* 23, 103803. <https://doi.org/10.1016/j.dib.2019.103803>.
- Khan, J., Wang, P., Xie, Y., Wang, L., Li, L., 2018. Mapping MODIS LST NDVI imagery for drought monitoring in Punjab Pakistan. *IEEE Access* 6, 19898–19911. <https://doi.org/10.1109/ACCESS.2018.2821717>.
- Khatako, R., Talchhabadel, R., Thapa, B.R., 2021. Evaluation of different precipitation inputs on streamflow simulation in Himalayan River basin. *J. Hydrol.* 599, 126390 <https://doi.org/10.1016/j.jhydrol.2021.126390>.
- Kumar, R.P., Prakash, A., Singh, R., Kumar, P., 2024a. Machine learning-based prediction of hazards fine PM2.5 concentrations: a case study of Delhi, India. *Discov. Geosci.* 2, 34. <https://doi.org/10.1007/s44288-024-00043-z>.
- Kumar, R.P., Singh, R., Kumar, P., Nahid, S., Singh, S.K., Nijjar, C.S., 2024b. Aerosol-PM2.5 Dynamics: In-situ and satellite observations under the influence of

- regional crop residue burning in post-monsoon over Delhi-NCR, India. Environ. Res. 255, 119141. <https://doi.org/10.1016/j.envres.2024.119141>.
- Lam, K.F., Mui, H.W., Yuen, H.K., 2001. A note on minimizing absolute percentage error in combined forecasts. Comput. Oper. Res. 28, 1141–1147. [https://doi.org/10.1016/S0305-0548\(00\)00026-5](https://doi.org/10.1016/S0305-0548(00)00026-5).
- Li, J., Song, C., Cao, L., Zhu, F., Meng, X., Wu, J., 2011. Impacts of landscape structure on surface urban heat islands: a case study of Shanghai, China. Remote Sens. Environ. 115, 3249–3263. <https://doi.org/10.1016/j.rse.2011.07.008>.
- Li, R., Zhu, G., Lu, S., Sang, L., Meng, G., Chen, L., Jiao, Y., Wang, Q., 2023. Effects of urbanization on the water cycle in the Shiyang River basin: based on a stable isotope method. Hydrol. Earth Syst. Sci. 27, 4437–4452. <https://doi.org/10.5194/hess-27-4437-2023>.
- Liu, J., Yang, K., Tariq, A., Lu, L., Soufan, W., El Sabagh, A., 2023. Interaction of climate, topography and soil properties with cropland and cropping pattern using remote sensing data and machine learning methods. Egypt. J. Remote Sens. Sp. Sci. 26, 415–426. <https://doi.org/10.1016/j.ejrs.2023.05.005>.
- Lizhou, W., Bo, H., Jianbing, P., 2024. Analysis of Rainfall-Caused Seepage into Underlying Bedrock Slope Based on Seepage Deformation Coupling. Int. J. Geomech. 24, 4024076. <https://doi.org/10.1061/IJGNALGMENG-9175>.
- Mathew, A., Khandelwal, S., Kaul, N., 2016. Spatial and temporal variations of urban heat island effect and the effect of percentage impervious surface area and elevation on land surface temperature: study of Chandigarh city, India. Sustain. Cities Soc. 26, 264–277. <https://doi.org/10.1016/j.scs.2016.06.018>.
- Montaner-Fernández, D., Morales-Salinas, L., Rodríguez, J.S., Cárdenas-Jirón, L., Huete, A., Fuentes-Jaque, G., Pérez-Martínez, W., Cabezas, J., 2020. Spatio-temporal variation of the urban heat island in Santiago, Chile during summers 2005–2017. Remote Sens. 12, 1–19. <https://doi.org/10.3390/rs12203345>.
- Naqvi, S.A.A., Sajjad, M., Tariq, A., Sajjad, M., Waseem, L.A., Karuppannan, S., Rehman, A., Hassan, M., Al-Ahmadi, S., Hatamleh, W.A., 2024. Societal knowledge, attitude, and practices towards dengue and associated factors in epidemic-hit areas: geoinformation assisted empirical evidence. Heliyon 10, e23151. <https://doi.org/10.1016/j.heliyon.2023.e23151>.
- Pal, S., Ziaul, S., 2017. Detection of land use and land cover change and land surface temperature in English Bazar urban centre. Egypt. J. Remote Sens. Sp. Sci. 20, 125–145. <https://doi.org/10.1016/j.ejrs.2016.11.003>.
- Qiao, Z., Wu, C., Zhao, D., Xu, X., Yang, J., Feng, L., Sun, Z., Liu, L., 2019. Determining the boundary and probability of surface urban heat island footprint based on a logistic model. Remote Sens. 11, 1–20. <https://doi.org/10.3390/rs11111368>.
- Qiu, S., Yang, H., Zhang, S., Huang, S., Zhao, S., Xu, X., He, P., Zhou, W., Zhao, Y., Yan, N., Nikolaidis, N., Christie, P., Banwart, S.A., 2023. Carbon storage in an arable soil combining field measurements, aggregate turnover modeling and climate scenarios. CATENA 220, 106708. <https://doi.org/10.1016/j.catena.2022.106708>.
- Qu, Y., Long, H., 2018. The economic and environmental effects of land use transitions under rapid urbanization and the implications for land use management. Habitat Int. 82, 113–121. <https://doi.org/10.1016/j.habitatint.2018.10.009>.
- Rahman, A., ur, Yasmeen, K., Islam, F., Anees, S.A., Tariq, A., Zubair, M., Bilal, M., Rahman, I.U., Rahman, S.U., Hatamleh, W.A., 2023. Assessment of heavy metal accumulation in dust and leaves of *Conocarpus erectus* in urban areas: implications for phytoremediation. Phys. Chem. Earth, Parts A/B/C 132, 103481. <https://doi.org/10.1016/j.pce.2023.103481>.
- Rivera, E., Antonio-Némiga, X., Origel-Gutiérrez, G., Sarricolea, P., Adame-Martínez, S., 2017. Spatiotemporal analysis of the atmospheric and surface urban heat islands of the Metropolitan Area of Toluca, Mexico. Environ. Earth Sci. 76 <https://doi.org/10.1007/s12665-017-6538-4>.
- Rouse, J.W., 1973. Monitoring vegetation systems in the great plains with erts. Remote Sensingcenter, Texas A&M hivemity. Colfegp Station. Texas Abstr 24, 309–317. <https://doi.org/10.1021/jf60203a024>.
- Shah, S.H.I.A., Yan, J., Ullah, I., Aslam, B., Tariq, A., Zhang, L., Mumtaz, F., 2021. Classification of aquifer vulnerability by using the drastic index and geo-electrical techniques. Water (Switzerland) 13. <https://doi.org/10.3390/w13162144>.
- Sheng, P., He, Y., Guo, X., 2017. The impact of urbanization on energy consumption and efficiency. Energy Environ. 28, 673–686. <https://doi.org/10.1177/0958305X17722389>.
- Sobrino, J.A., Oltra-Carrió, R., Sòria, G., Bianchi, R., Paganini, M., 2012. Impact of spatial resolution and satellite overpass time on evaluation of the surface urban heat island effects. Remote Sens. Environ. 117, 50–56. <https://doi.org/10.1016/j.rse.2011.04.042>.
- Sriwanit, M., Hokao, K., Phonekeo, V., 2012. Assessing the impact of urbanization on urban thermal environment: a case study of bangkok metropolitan. Int. J. Appl. Sci. Technol. 2, 243–256.
- Sun, L., Wang, X., Zheng, Y., Wu, Z., Fu, L., 2024. Multiscale 3-D–2-D Mixed CNN and Lightweight Attention-Free Transformer for Hyperspectral and LiDAR Classification. IEEE Trans. Geosci. Remote Sens. 62, 1–16. <https://doi.org/10.1109/TGRS.2024.3367374>.
- Tariq, A., Shu, H., 2020. CA-Markov chain analysis of seasonal land surface temperature and land use landcover change using optical multi-temporal satellite data of Faisalabad, Pakistan. Remote Sens. 12, 1–23. <https://doi.org/10.3390/rs12203402>.
- Tariq, A., Riaz, I., Ahmad, Z., Yang, B., Amin, M., Kausar, R., Andleeb, S., Farooqi, M.A., Rafiq, M., 2020. Land surface temperature relation with normalized satellite indices for the estimation of spatio-temporal trends in temperature among various land use land cover classes of an arid Pothohar region using Landsat data. Environ. Earth Sci. 79, 40. <https://doi.org/10.1007/s12665-019-8766-2>.
- Tariq, A., Shu, H., Siddiqui, S., Imran, M., Farhan, M., 2021a. Monitoring land use and land cover changes using geospatial techniques, A case study of fateh jang, attock, Pakistan. Geogr. Environ. Sustain. 14, 41–52. <https://doi.org/10.24057/2071-9388-2020-117>.
- Tariq, A., Shu, H., Siddiqui, S., Munir, I., Sharifi, A., Li, Q., Lu, L., 2021b. Spatio-temporal analysis of forest fire events in the Margalla Hills, Islamabad, Pakistan using socio-economic and environmental variable data with machine learning methods. J. For. Res. 13, 12. <https://doi.org/10.1007/s11676-021-01354-4>.
- Tariq, A., Siddiqui, S., Sharifi, A., Shah, S.H.I.A., 2022a. Impact of spatio-temporal land surface temperature on cropping pattern and land use and land cover changes using satellite imagery, Hafizabad District, Punjab, Province of Pakistan. Arab. J. Geosci. 15, 1045. <https://doi.org/10.1007/s12517-022-10238-8>.
- Tariq, A., Yan, J., Mumtaz, F., 2022b. Land change modeler and CA-Markov chain analysis for land use land cover change using satellite data of Peshawar, Pakistan. Phys. Chem. Earth, Parts A/B/C 128, 103286. <https://doi.org/10.1016/j.pce.2022.103286>.
- Tariq, A., Jiango, Y., Li, Q., Gao, J., Lu, L., Soufan, W., Almutairi, K.F., Habib-ur-Rahman, M., 2023. Modelling, mapping and monitoring of forest cover changes, using support vector machine, kernel logistic regression and naive bayes tree models with optical remote sensing data. Heliyon 9, e13212. <https://doi.org/10.1016/j.heliyon.2023.e13212>.
- Tomlinson, C.J., Chapman, L., Thornes, J.E., Baker, C.J., 2012. Derivation of Birmingham's summer surface urban heat island from MODIS satellite images. Int. J. Climatol. 32, 214–224. <https://doi.org/10.1002/joc.2261>.
- Tufail, M., Nasir, M.J., Tariq, A., Ali, Z., Alarifi, S.S., 2024. Assessing access to safe drinking water in flood-affected areas of District Nowshera, Pakistan: A case study towards achieving sustainable development goal 6.1. Ecohydrol. Hydrobiol. <https://doi.org/10.1016/j.ecohyd.2024.07.001>.
- Wahila, S., Kazmi, J.H., Sharifi, A., Shirazi, S.A., Tariq, A., Joyell Smith, H., 2022. Assessing spatio-temporal mapping and monitoring of climatic variability using SPEI and RF machine learning models. Geocarto Int. 37, 14963–14982. <https://doi.org/10.1080/10106049.2022.2093411>.
- Wunsch, A., Liesch, T., Broda, S., 2021. Groundwater level forecasting with artificial neural networks: a comparison of long short-term memory (LSTM), convolutional neural networks (CNNs), and non-linear autoregressive networks with exogenous input (NARX). Hydrol. Earth Syst. Sci. 25, 1671–1687. <https://doi.org/10.5194/hess-25-1671-2021>.
- Yin, L., Wang, L., Keim, B.D., Koosner, K., Yin, Z., Liu, M., Zheng, W., 2023a. Spatial and wavelet analysis of precipitation and river discharge during operation of the Three Gorges Dam, China. Ecol. Indic. 154, 110837. <https://doi.org/10.1016/j.ecolind.2023.110837>.
- Yin, L., Wang, L., Li, T., Lu, S., Tian, J., Yin, Z., Li, X., Zheng, W., 2023. U-Net-LSTM: time series-enhanced lake boundary prediction model. Land. <https://doi.org/10.3390/land12101859>.
- Yin, L., Wang, L., Li, T., Lu, S., Yin, Z., Liu, X., Li, X., Zheng, W., 2023. U-Net-STN: A Novel End-to-End Lake Boundary Prediction Model. Land 12, 1602. <https://doi.org/10.3390/land12081602>.
- Yu, B., Zhou, X., 2024. Land finance and urban Sprawl: Evidence from prefecture-level cities in China. Habitat Int. 148, 103074. <https://doi.org/10.1016/j.habitatint.2024.103074>.
- Zhang, K., Li, Y., Yu, Z., Yang, T., Xu, J., Chao, L., Ni, J., Wang, L., Gao, Y., Hu, Y., Lin, Z., 2022. Xin'anjiang Nested Experimental Watershed (XAJ-NEW) for Understanding Multiscale Water Cycle. Scientific Objectives and Experimental Design. Engineering 18, 207–217. <https://doi.org/10.1016/j.eng.2021.08.026>.
- Zhao, Yang, Li, J., Wang, Y., Zhang, W., Wen, D., 2024a. Warming Climate-Induced Changes in Cloud Vertical Distribution Possibly Exacerbate Intra-Atmospheric Heating Over the Tibetan Plateau. Geophys. Res. Lett. 51 e2023GL107713. <https://doi.org/10.1029/2023GL107713>.
- Zhao, Yang, Lu, M., Chen, D., Zhang, L., 2024b. Understanding the weakening patterns of inner Tibetan Plateau vortices. Environ. Res. Lett. 19, 064076. <https://doi.org/10.1088/1748-9326/ad5193>.
- Zhao, Ying, Yi, J., Yao, R., Li, F., Hill, R.L., Gerke, H.H., 2024. Dimensionality and scales of preferential flow in soils of Shale Hills hillslope simulated using HYDRUS. Vadose Zo. J 1–24. <https://doi.org/10.1002/vzj2.20367>.
- Zhou, G., Li, H., Song, R., Wang, Q., Xu, J., Song, B., 2022. Orthorectification of Fisheye Image under Equidistant Projection Model. Remote Sens. <https://doi.org/10.3390/rs14174175>.
- Zhou, G., Liu, X., 2022. Orthorectification Model for Extra-Length Linear Array Imagery. IEEE Trans. Geosci. Remote Sens. 60, 1–10. <https://doi.org/10.1109/TGRS.2022.3223911>.
- Zhou, G., Tang, Y., Zhang, W., Liu, W., Jiang, Y., Gao, E., Zhu, Q., Bai, Y., 2023. Shadow Detection on High-Resolution Digital Orthophoto Map Using Semantic Matching. IEEE Trans. Geosci. Remote Sens. 61, 1–20. <https://doi.org/10.1109/TGRS.2023.3294531>.